PAPER

Check for updates

Short-peptide based supramolecular nanocomposite hydrogels for the disruption of polymicrobial biofilms and accelerated infected wound healing

Sudip Mukherjee, [iD] †[a] Manuel Núñez-Martínez, [iD] †[b] Sara Illescas-Lopez, [iD] [b] Archanna Jeyakumar, [iD] [b,e] Modesto Torcuato Lopez-Lopez, [iD] [c,d] Juan Manuel Cuerva, [iD] [b] Vaibhav Bhatia,[e] José Antonio Gavira,[f] Luis Álvarez de Cienfuegos [iD] *[b,d] and Jayanta Haldar [iD] *[a,g]

The escalating prevalence of drug-resistant microbes coupled with their persistence in mono- and poly-microbial biofilms impose a critical healthcare challenge. Metal nanoparticles, particularly silver nanoparticles (AgNPs) and gold nanoparticles (AuNPs), offer potent antimicrobial activity but face limitations due to their complex synthetic protocols, reliance on external reducing agents and surfactants, resulting compromised biocompatibility and poor *in vivo* outcomes. Herein, we present a facile, biocompatible approach for synthesizing antimicrobial supramolecular nanocomposite hydrogels (ASNH) *via* a one-pot, aqueous process that enables *in situ* growth of AgNPs and AuNPs through supramolecular interactions with short peptides. Utilizing sunlight photoirradiation, these hydrogels eliminate external reducing agents while serving as stabilizers for nanoparticle formation. The metallohydrogels exhibit rapid and broad-spectrum antimicrobial activity, against multidrug resistant bacteria and fungi. In addition to disrupting single species biofilms, the optimal hydrogels significantly eradicate polymicrobial biofilms formed by MRSA and *Candida albicans*. The hydrogels achieve ≥1.5-log reduction in microbial viability, outperforming last resort antibiotics and commercial silver-based ointments. *In vivo* studies demonstrate accelerated wound healing by reducing bacterial burden and mitigating inflammatory responses, while enhancing neovascularization, granulation, fibroblast proliferation, collagen deposition and epithelialization. The mild, economical synthesis and robust antimicrobial efficacy of these peptide-based metallohydrogels underscore their clinical potential as next-generation biomaterials for polymicrobial biofilm-associated infections.

[a]Antimicrobial Research Laboratory, New Chemistry Unit, Jawaharlal Nehru Centre for Advanced Scientific Research, Jakkur, Bengaluru-560064, Karnataka, India. E-mail: jayanta@jncasr.ac.in

[b]Universidad de Granada (UGR), Departamento de Química Orgánica, Unidad de Excelencia Química Aplicada a Biomedicina y Medioambiente (UEQ), C. U. Fuentenueva, Avda. Severo Ochoa s/n, E-18071 Granada, Spain. E-mail: lac@ugr.es

[c]UGR, Departamento de Física Aplicada, C. U. Fuentenueva, Avda. Severo Ochoa s/n, E-18071 Granada, Spain

[d]Instituto de Investigación Biosanitaria ibs.GRANADA, Av. De Madrid, 15, 18016 Granada, Spain

[e]Lamark Biotech Pvt. Ltd, BS5, 1st floor, NIP900, NCL Innovation Park, Dr Homi Bhabha Rd, Pune-411008, Maharashtra, India

[f]Laboratorio de Estudios Cristalográficos, Instituto Andaluz de Ciencias de la Tierra, Consejo Superior de Investigaciones Científicas, Avenida de las Palmeras 4, 18100 Armilla, Granada, Spain

[g]School of Advanced Materials, Jawaharlal Nehru Centre for Advanced Scientific Research, Jakkur, Bengaluru-560064, Karnataka, India

† These authors contributed equally to this work.

1. Introduction

Over the past decades, the alarming surge of multidrug-resistant bacterial strains synchronized with the prevalence of fungal infections has emerged as a serious global healthcare challenge, further jeopardized by the scarcity of novel therapeutic candidates.[1–6] The crisis is aggravated by the formation of microbial biofilms in almost all possible biotic and abiotic surfaces.[7,8] Compounding this nightmare, a majority of these biofilms acts as a niche/scaffold attracting other microbes and resulting in a formation of polymicrobial (bacteria and fungi) or multi-species bacterial (Gram-positive and Gram-negative bacteria) biofilms.[9–11] The inter-kingdom interactions between fungi and bacteria play a crucial role in altered colonisation, virulence, and susceptibility to both host immune responses and existing antimicrobial agents, rendering traditional therapies ineffective. Therefore, there is an urgent need to develop

novel broad-spectrum therapeutics and biomaterials capable of combating bacteria, fungi, and polymicrobial infections with potent biocompatibility.

Among different classes of broad-spectrum antimicrobials, metal nanoparticles, in particular AgNPs, have shown strong microbicidal activity towards a wide range of bacteria, fungi and viruses, being less susceptible to microbial resistance.[12–17] Silver increases the permeability of microbial cells and inactivates enzymes and DNA through its coordination with electron-rich groups.[12,18] Silver-based formulations have been explored in multiple forms, such as soluble salts, in nanoparticles, and in combination with different carriers such as polymers, *etc.*[19] Nevertheless, AgNPs have shown cellular toxicity when used at high doses or prolonged time.[20] Thus, the development of more biocompatible broad-spectrum microbicides by simpler and cost-effective protocols is desired. In this sense, the use of hydrogels loaded with antibacterial agents or with intrinsic antibacterial activity can be a good strategy as hydrogels can be highly biocompatible and biodegradable.[21–23] In particular, short-peptide supramolecular hydrogels based on aromatic peptides have shown promising applications in this field, as some peptides have intrinsic antibacterial activity[24] and others have been used to obtain AgNPs by mild methods[25] with excellent antibacterial properties.[26] These peptides can form a hydrogel under very mild conditions, promoting peptide self-assembly by the addition of metallic salts, a change in the pH or solvent, or mediation by the action of enzymes.[27,28] These hydrogels can be made more biocompatible in combination with natural polymers such as collagen, hyaluronic acid, fibrin, *etc.*[29–34] and/or bioactive peptide fragments, such as RGD (arginine–glycine–aspartic acid) shown to promote cell adhesion.[33,35] Additionally, these peptides have also been shown to be excellent media to occlude and disperse different inorganic and carbon-based particles[36–41] and to promote the growth of different crystalline compounds by a mild process.[42–47]

Based on this hypothesis, herein, we have prepared antimicrobial supramolecular nanocomposite hydrogels (ASNHs) with different short-peptides and metal nanoparticle composites with the final goal of obtaining biocompatible biomaterials having potent antimicrobial activity. For this purpose, we have combined Fmoc-FF (Fmoc-diphenylalanine)/Fmoc-RGD (Fmoc-arginine–glycine–aspartic acid)/collagen with AgNPs and AuNPs. It is interesting to note that the antibacterial properties of AuNPs have been significantly less studied when compared with those of AgNPs, as well as mild methods used to obtain them.[17,22,48,49] In this case, these hydrogels were capable of producing both types of metallic nanoparticles by a simple sunlight photoirradiation methodology avoiding the use of external reducing agents that could affect the biocompatibility of the system. Composite hydrogels acted as capping and stabilizing nanoparticle agents. The incorporation of Fmoc-RGD and collagen made the hydrogel more biocompatible and exerted control over the particle size and morphology. *In situ* formation of metallic nanoparticles within the peptide fibers did not disturb the mechanical properties of the resulting composite metallohydrogels. Composite hydrogels possessing rapid antimicrobial activity and low hemolytic activity were optimized. The rapid and broad-spectrum antimicrobial activity of the optimized hydrogels was investigated along with the detailed elucidation of their microbicidal mechanism of action. Furthermore, the efficacy of these hydrogels to disrupt bacterial and fungal biofilms as well as their co-existence in polymicrobial biofilms were also assessed. Finally, *in vivo* wound healing ability and antimicrobial properties were investigated in a mouse model of excisional wound infection.

2. Results and discussion

2.1 Design, characterization, and antibacterial properties of antimicrobial supramolecular nanocomposite hydrogels (ASNHs)

At first, we tested the gelation ability of Fmoc-FF through simple addition of silver ($AgNO_3$, 100 mM) and gold ($HAuCl_4$, 100 mM) salts. For this purpose, aqueous solutions of Fmoc-FF (10 mM) were prepared by the addition of NaOH, and to these solutions, different concentrations (0.1–7 mM) of $AgNO_3$ or $HAuCl_4$ were added (Fig. 1A). Lower concentrations (0.1, 0.5 and 1 mM) of $AgNO_3$ or $HAuCl_4$ did not lead to hydrogel formation. 3 mM $AgNO_3$ or $HAuCl_4$, which was the minimum concentration required to trigger hydrogel formation, was added (Fig. 1B). Then the samples were exposed to sunlight to induce metal nanoparticle formation following a described protocol[25] (ASNH-1, ASNH-2, and ASNH-3 containing AgNPs and ASNH-7, ASNH-8, and ASNH-9 containing AuNPs did not form hydrogels, whereas ASNH-4, ASNH-5, and ASNH-6 containing AgNPs and ASNH-10, ASNH-11, and ASNH-12 containing AuNPs formed hydrogels). After 24 hours, the hydrogels showed a change in color from translucid to dark brown (for AgNPs) or black (for AuNPs), indicating the formation of metallic nanoparticles (Fig. 1A).[50] Transmission electron microscopy (TEM) of dried hydrogels confirmed the formation of AgNPs and AuNPs where the sizes were around 3.9 ± 0.7 nm for AgNPs and 19 ± 4 nm for AuNPs (Fig. 1Ci and Cii). In the case of AuNPs, other morphologies besides spheres, such as triangular particles, were also observed. AgNPs appeared highly associated with the peptide fibers, confirming the role of Fmoc-FF as a reducing and stabilizing agent (Fig. 1Ci). After preparing the ASNH-AgNP and ASNH-AuNP hydrogels, a preliminary screening of their antibacterial activity was performed against a Gram-positive bacterium methicillin resistant *Staphylococcus aureus* (MRSA ATCC 33591) and a Gram-negative bacterium *Escherichia coli* (MTCC 443). All the hydrogels showed potent activity against both the bacteria. They eliminated the bacterial burden, exhibiting ~6 log reduction within 12 hours of incubation (Fig. 1D).

2.2 Engineering biocompatible Fmoc-FF/Fmoc-RGD/collagen nanocomposite hydrogels with silver and gold nanoparticles

Considering the potential toxicity of AgNPs, we decided to develop more biocompatible hydrogels by incorporating Fmoc-
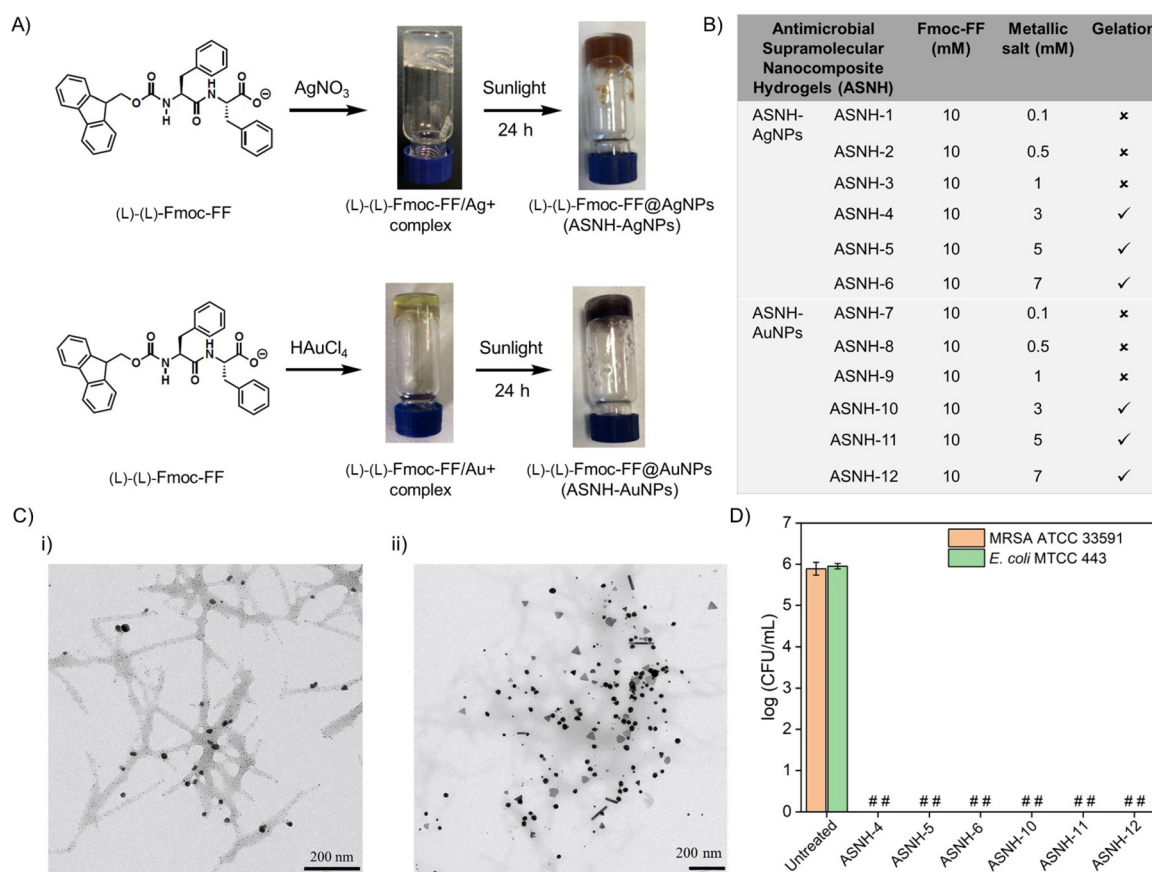
Fig. 1 Synthetic scheme for the preparation of antimicrobial supramolecular nanocomposite hydrogels (ASNH) containing silver nanoparticles (ASNH-AgNPs) and gold nanoparticles (ASNH-AuNPs). (B) Tabular summary of the components: Fmoc-diphenylalanine (Fmoc-FF) and metallic salts (AgNO$_3$ and HAuCl$_4$), used to prepare the hydrogels. (✗) corresponds to no hydrogel formation and (✓) indicates hydrogel formation. (C) TEM images of (i) ASNH-4 and (ii) ASNH-10 hydrogels. (D) Antibacterial activity of the hydrogels against MRSA ATCC 33591 and *E. coli* MTCC 443 after 12 h of incubation. '#' corresponds to <50 CFU mL^{-1}.

RGD and collagen, both components known for their *in vivo* biocompatibility and capacity to promote cell adhesion and growth (Fig. S1A).[34,35] Moreover, the incorporation of Fmoc-RGD, an acidic peptide, promotes gelation allowing the reduction of the concentration of silver salt below 3 mM. For this purpose and based on our previous experience,[33,38] a composite hydrogel (Antimicrobial Supramolecular Hydrogel (ASH)) made of Fmoc-FF (20 mM), Fmoc-RGD (20 mM) and collagen (3 mg mL^{-1}) in a ratio 3.5 : 1.5 : 5 was prepared (Fig. S1A and S1B). Interestingly, the polar groups present in the amino acid residues of ASNH can act as interaction points for Ag and AuNPs and make them interesting candidates for their stabilization.[51,52] The hydrogel was characterized by different electron microscopy techniques. TEM images of the composite hydrogels showed the characteristic Fmoc-peptide fibers several microns in length, suggesting that the presence of collagen in the mixture did not significantly alter peptide self-assembly or supramolecular hydrogel formation (Fig. S1C). ESEM images revealed the presence of some spherical aggregates distributed within the sheets. These aggregates were not observed in Fmoc-peptide gels[37] and could be the result of the

incorporation of collagen in the mixture (Fig. S1D). The FT-IR spectrum showed characteristics of Fmoc-dipeptide bands, such as amide I bands at 1692 cm^{-1} (this one ascribed to the stacking of the carbamate groups) and 1652 cm^{-1} and an amide II band at 1534 cm^{-1}, both signals indicative of a β-sheet arrangement (Fig. 2F). The incorporation of collagen, in addition to presenting amide I and II bands superimposed with the Fmoc-dipeptides, provides new signals also related to the secondary structure of the triple helix of collagen as the band at 1445 cm^{-1} and the amide III band at 1256 cm^{-1}, the latter blue-shifted with respect to the one reported at 1240 cm^{-1}.[53] This amide III band is attributed to hydrogen bonds between strands in the triple helix, and their displacement in the composite could be due to an alteration of the hydrogen bond pattern because of the presence of Fmoc-peptides. Other amide III bands at 1287 cm^{-1} and 1201 cm^{-1} are also characteristic of the collagen triple helix (Fig. 2F).

The rheological tests under oscillatory shear stress of constant frequency and increasing amplitude (amplitude sweeps) of the hydrogel showed typical trends of viscoelastic gel-like behavior (Fig. S1E). These trends are characterized by ampli-
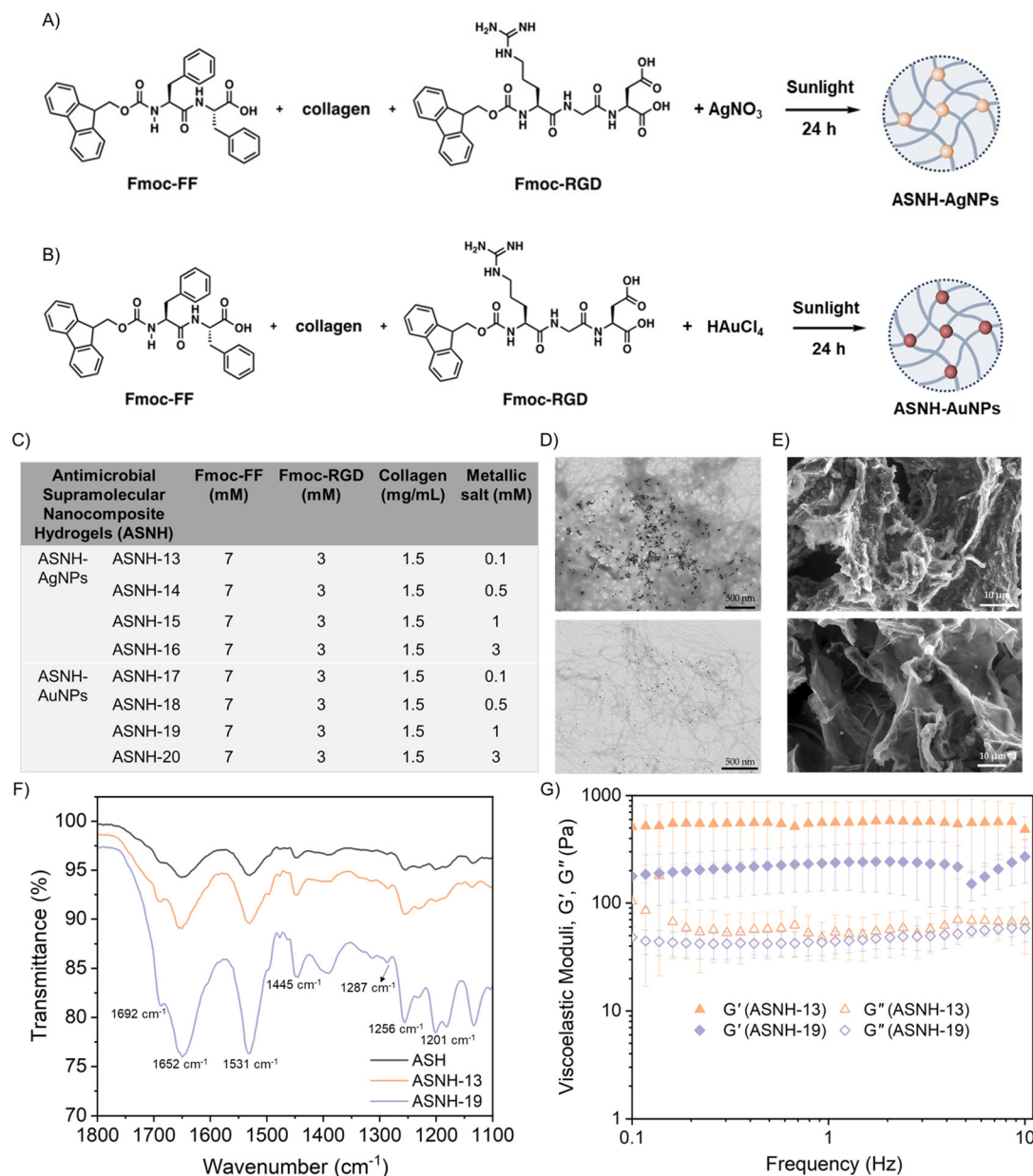
Fig. 2 Synthetic scheme for *in situ* growth of (A) AgNPs and (B) AuNPs in composite hydrogels containing Fmoc-FF, Fmoc-RGD and collagen. (C) Tabular summary of the components Fmoc-FF, Fmoc-RGD, collagen and metallic salts (AgNO$_3$ and HAuCl$_4$) used to prepare the hydrogels. (D) TEM image of the composite hydrogel with ASNH-AgNPs (ASNH-13, upper panel) and ASNH-AuNPs (ASNH-19, bottom panel). (E) ESEM image of the composite hydrogel with ASNH-AgNPs (ASNH-13, upper panel) and ASNH-AuNPs (ASNH-19, bottom panel). (F) FT-IR spectra of the composite hydrogels ASH, ASNH-13 and ASNH-19. (G) Mechanical properties of the hydrogels under oscillatory stress of fixed amplitude and increasing frequency (frequency sweeps).

tude-independent values of both the storage modulus (G') and the loss modulus (G''), with $G' > G''$ at low stress amplitude, which defines the linear viscoelastic region (LVR), followed by a sharp decrease of both moduli above a critical value of stress amplitude that defines the onset of the nonlinear viscoelastic region, where the sample undergoes breakage (Fig. S1E). A more complete picture of the mechanical behavior of the hydrogel is obtained by analyzing its response under oscillatory shear stress of constant amplitude within the LVR and

increasing frequency, a test known as frequency sweep. The results of this test show values of both G' and G'' almost independent of frequency, with G' larger than G'' by slightly less than an order of magnitude (Fig. S2A). Frequency independence is typical of hydrogels with a clear gel-like mechanical behavior, but the fact that G' is less than one order of magnitude larger than G'' defines a weak gel.

Next, to a solution of Fmoc-FF and collagen different concentrations of silver (AgNO$_3$) and gold (HAuCl$_4$) salts (from 0.1

to 3 mM of Au^{3+} and Ag^+) were added. Gel formation was triggered by the addition of Fmoc-RGD (Fig. 2A and B) allowing the reduction of the metallic salt concentration. For all the composite metallohydrogels prepared, the concentration and proportion of the peptides were always the same and identical to those of the sample without metal salts (Fig. 2C). Following the same protocol applied to Fmoc-FF and silver, composite hydrogels containing silver and gold salts were exposed to sunlight for 24 hours. After these 24 hours of irradiation, the color of the hydrogels changed dramatically confirming the formation of nanoparticles (ASNH-AgNPs: ASNH-13, ASNH-14, ASNH-15, and ASNH-16 and ASNH-AuNPs: ASNH-17, ASNH-18, ASNH-19, and ASNH-20). In the case of AgNPs, it turned from white–transparent to yellow (Fig. S2B) and for the AuNPs it turned from pale yellow to intense red (Fig. S2C). UV-Visible spectra of hydrogels containing AgNPs showed the presence of a localized surface plasmon resonance band (LSPR) centered at 441 nm corresponding to the formation of spherical nanoparticles (Fig. S2D). On the other hand, hydrogels containing AuNPs showed an LSPR band at 545 nm associated with the formation of spherical AuNPs (Fig. S2E). Composite hydrogels containing silver and gold salts (0.1 mM) were characterized by TEM images, showing in both cases the formation of spherical nanoparticles within the hydrogel fibers (Fig. 2D). In the case of AgNPs, statistical data reveal the formation of spherical nanoparticles with an average size of 19 ± 4 nm (Fig. 2D, upper panel). For AuNPs, the statistical analysis showed the formation of nanoparticles with a spherical morphology and diameters of 6 ± 2 nm (Fig. 2D, bottom panel). Unlike hydrogels with Fmoc-FF + AuNPs (ASNH-19), in this case, the polymorphism of the sample was inhibited, finding only spherical nanoparticles. This may be due to the presence of a greater number of amino acids (RGD and collagen) that can interact with gold. ESEM images showed a broad and homogeneous distribution of metallic nanoparticles within the peptide structure (Fig. 2E). EDX studies of the same samples confirmed the presence of gold and silver in the hydrogel structure (Fig. S4). FT-IR spectra for both metallohydrogels showed similar spectra to that of the ASH (control), confirming that the formation of the nanoparticles within the hydrogels did not alter the β-sheet supramolecular arrangement (Fig. 2F).

Subsequently, the water uptake and retention capacities of the hydrogels were evaluated. For wound healing applications, maintaining a moist environment and ensuring high oxygen permeability are two critical requirements. The equilibrium water content (EWC) of ASNH-13 and ASNH-19 was first measured, and both hydrogels exhibited exceptionally high water contents of 96–97% (Fig. S3A). This confirms their potential to maintain wound moisture and enhance oxygen transport. The water retention ability of the hydrogels was then assessed. Since water retention is closely associated with the elasticity of hydrogels—where higher water content generally corresponds to a softer and more flexible gel—this property is particularly relevant. ASNH-13 and ASNH-19 retained ~50% water even after 6 hours and 4 hours, respectively (Fig. S3B). This indicates that ASNH-13 retains water for a longer duration

compared to ASNH-19. The superior retention of ASNH-13 is likely due to its smaller pore size, which reduces water loss over time. The swelling behavior of the hydrogels was also analyzed. ASNH-13 showed a swelling ratio of >5, whereas ASNH-19 exhibited >13 times swelling compared to its dry weight, validating that these hydrogels can absorb a large amount of wound fluids (Fig. S3C). However, with time the swelling ratio decreased, indicating disintegration of the gels during extended incubation in PBS at 37 °C (Fig. S3C). This degradation can be attributed to the supramolecular nature of the hydrogels. In the absence of chemical crosslinkers during gelation, drying processes may have collapsed the polymeric network, making the hydrogels porous, brittle, and mechanically weaker. Consistent with its higher porosity, ASNH-19 displayed a greater initial swelling before undergoing disintegration.

Upon investigation of the mechanical properties, composite hydrogels (ASNH-13 and ASNH-19) showed similar trends to the control hydrogel (ASH) without metal NPs both in terms of frequency sweeps (Fig. 2G) and amplitude sweeps (Fig. S2F). Therefore, similar conclusions could be drawn that these hydrogels behave like typical weak gels. The only remarkable difference was in the magnitude of both G' and G'' compared to that of the sample without AuNPs or AgNPs. In this regard, the presence of AgNPs significantly enhanced the robustness of the ASNH-13 hydrogel, as evidenced by the increased values of G' and G''. In contrast, the presence of AuNPs slightly weakened the hydrogel (ASNH-19), although this effect was within the standard deviation. This difference may be attributed to the higher concentration of AuNPs—approximately ten times greater than that of AgNPs. Previous studies have consistently reported that the incorporation of NPs can enhance the mechanical strength of hydrogels by acting as crosslinking nodes or structural supports within the 3D network.[37,54] However, several reports have also noted that beyond a critical NP concentration, the mechanical reinforcement effect diminishes or even reverses, leading to a decrease in strength. This phenomenon has been observed in both polymeric and peptide-based hydrogels.[37,54,55] The underlying mechanism is likely related to the excessive disruption of the polymeric or peptide network caused by high nanoparticle concentrations, which compromises the structural integrity of the hydrogel and ultimately reduces its mechanical strength.

2.3 Supramolecular nanocomposite hydrogels exhibit rapid, dose-dependent antibacterial activity with minimal hemolysis

The antibacterial activity of the synthesized hydrogels was tested against MRSA and *E. coli* in a time dependent manner. The composite hydrogel (ASH) without metal nanoparticles was completely ineffective in reducing the bacterial count (Fig. 3A and B). AgNPs containing hydrogels (ASNH-13, ASNH-14, ASNH-15 and ASNH-16) showed rapid killing kinetics, eliminating both the tested pathogens within 6 h of incubation (Fig. 3A and B). The killing kinetics was observed to be dose dependent. Hydrogels with relatively higher AgNP content: ASNH-14 and ASNH-15 (made of 0.5 mM and 1 mM
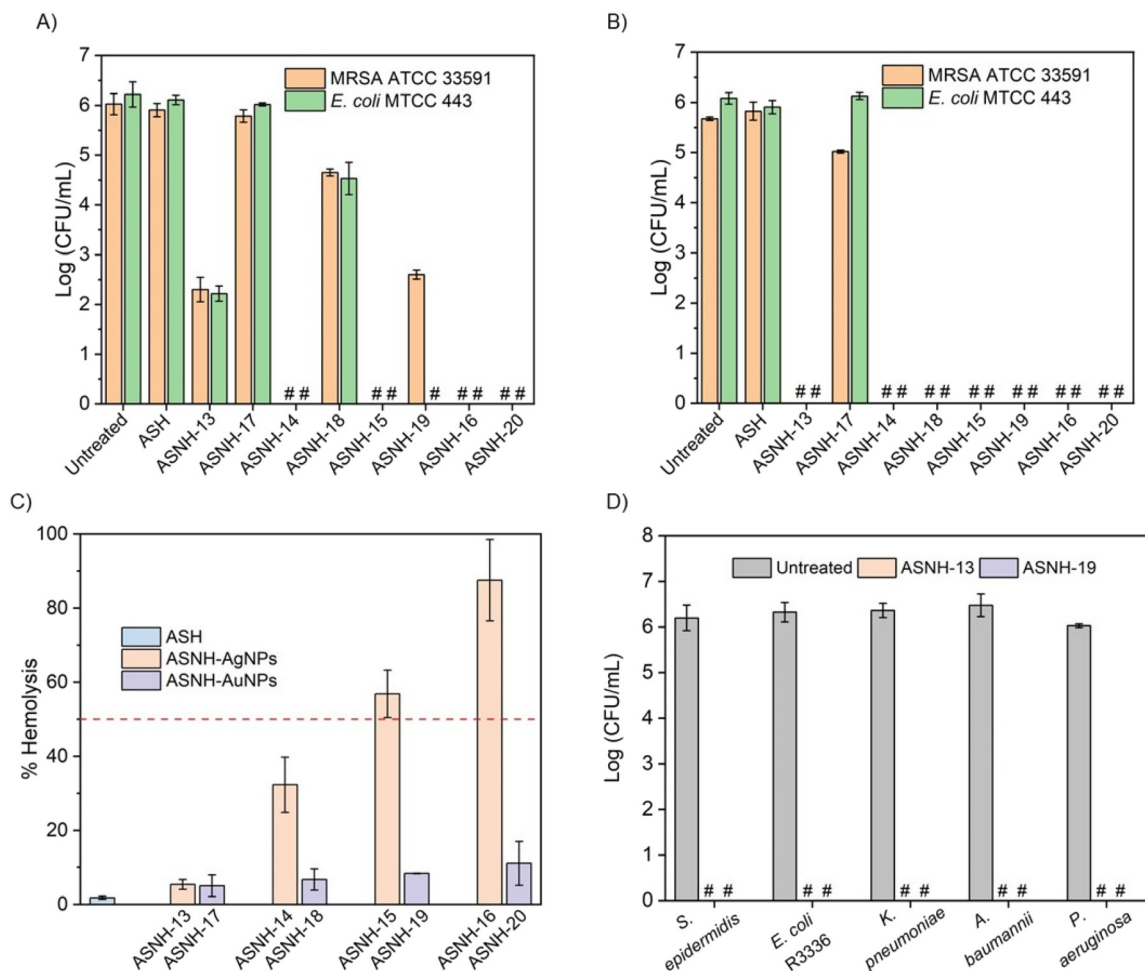
Fig. 3 (A) Antibacterial activity of ASH, ASNH-AgNP and ASNH-AuNP hydrogels against MRSA ATCC 33591 and *E. coli* MTCC 443 after (A) 3 h and (B) 6 h of incubation. (C) Hemolysis of the ASH, ASNH-AgNP and ASNH-AuNP hydrogels. (D) Antibacterial activity of optimized ASNH-13 and ASNH-19 against *S. epidermidis* MTCC 3615, *E. coli* R3336, *K. pneumoniae* R3934, *A. baumannii* R674 and *P. aeruginosa* R590 after 6 h of incubation. '#' corresponds to <50 CFU mL^{-1}.

Ag salt, respectively) caused ∼6 log reductions within 3 h of incubation against both the bacteria. On the other hand, hydrogels with AuNPs (ASNH-17, ASNH-18, ASNH-19 and ASNH-20) displayed relatively slower killing kinetics (Fig. 3A). The ASNH-19 hydrogel (made of 1 mM Au salt) AuNPs took 6 h to eliminate both the bacterial cells. However, against *E. coli*, it was able to completely eradicate the bacterial cells within 3 h of incubation (Fig. 3A). The relatively faster killing kinetics of metal nanoparticles against Gram-negative bacteria is well-reported in the literature.[12,17,18,56] The ASNH-17 hydrogel (made of 0.1 mM Au salt) displayed inferior antibacterial activity compared to its AgNP counterpart, proving superior antibacterial activity of AgNPs.

Subsequently, the toxicity of composite metallohydrogels was tested against human red blood cells (hRBCs). The control hydrogel, ASH, devoid of metal nanoparticles did not show any toxicity towards human erythrocytes (Fig. 3C). However, it was observed that upon increasing the nanoparticle concentration, the toxicity of the ASNH-AgNP hydrogels increased signifi-

cantly. In contrast, hydrogels with AuNPs displayed minimal toxicity even after increasing the Au content. This result is not unexpected as it is known that AuNPs are more stable than AgNPs.[57] The toxicity of the ASNH-15 hydrogel made of 1 mM Ag salt exhibited a substantially high hemolysis of 57 ± 6%, whereas the ASNH-19 hydrogel prepared from the same amount of Au salt showed only 8 ± 1% (Fig. 3C). Upon increasing the silver content further, the toxicity of the hydrogels increased drastically (87 ± 10% for ASNH-16). In contrast, a hydrogel synthesized with a similar concentration of Au salt (ASNH-20) displayed much lower hemolysis, only ∼11 ± 6%. The relatively higher reactivity of Ag salts with the cell membrane compared to that of Au salt resulted in higher toxicity of ASNH-AgNP hydrogels.[12,56] Therefore, after considering the extent of hemolysis and time–kill kinetics against both MRSA and *E. coli*, ASNH-13 (made of 0.1 mM Ag salt) and ASNH-19 (made of 1 mM Au salt) hydrogels were selected as the optimal formulations. After the initial optimization, the antibacterial activity of the selected hydrogels was tested against drug-resist-

ant bacterial strains commonly associated with wound infections such as *Staphylococcus epidermidis*, *E. coli Klebsiella pneumoniae*, *Acinetobacter baumannii* and *Pseudomonas aeruginosa*. Both the hydrogels exhibited rapid killing kinetics, causing ~6 log bacterial reduction for all the tested pathogens within 6 h of incubation (Fig. 3D). The rapid and selective antibacterial activity of the optimized hydrogels highlights their potential application as broad-spectrum antibacterial agents after 12 h of incubation.

2.4 Multifaceted bactericidal mechanisms of nanocomposite hydrogels: ROS generation, membrane depolarization, and permeabilization

To gain insight into the mechanism of bactericidal activity of the hydrogels, a series of microscopic and spectroscopic experiments were performed.

Production of intracellular reactive oxygen species (ROS). Metal nanoparticles such as AgNPs and AuNPs interact with the thiol and amino groups of proteins, with nucleic acids, and with cell membranes to generate reactive oxygen species (ROS).[12,56] Excessive ROS production, including superoxide and hydroxyl radicals, is a critical reason for bacterial cell death, as it causes widespread intracellular damage. Hydroxyl radicals, for instance, can induce DNA breaks, lipid peroxidation, and protein carbonylation, disrupting cellular integrity. To assess ROS generation in MRSA cells upon treatment with

the hydrogels, the ROS-sensitive dye 2′,7′-dichlorofluorescein diacetate (DCFH-DA) was used. This non-fluorescent, cell-permeable molecule is hydrolyzed intracellularly and reacts with ROS to form DCF, a fluorescent compound.[58] A significant increase in fluorescence intensity in treated cells compared to those of untreated controls confirmed intracellular ROS generation (Fig. 4A). The ASNH-13 hydrogel, prepared from a lower Ag salt concentration (0.1 mM), induced higher ROS levels than the ASNH-19 hydrogel made with a relatively higher Au salt concentration (1 mM). This increased ROS production is attributed to the superior reactivity of AgNPs, facilitating greater interaction with bacterial cellular components.[56] These findings collectively demonstrate that the hydrogels induce intracellular ROS production, a key mechanism responsible for bacterial cell death.

Membrane depolarizing ability. ROS generation can directly lead to membrane lipid peroxidation in bacterial cells, disrupting the membrane's structure and function due to the free radical chain reactions.[59,60] Damaged lipids can alter the fluidity and integrity of the cell membrane, affecting transport processes and potentially leading to cellular leakage. This alteration in ion homeostasis leads to an alteration in the membrane potential which was investigated using the membrane-potential sensitive dye 3,3′-dipropylthiadicarbocyanine iodide [DiSC$_3$ (5)]. The dye distributes both inside and outside microbial cells under normal membrane potential conditions.
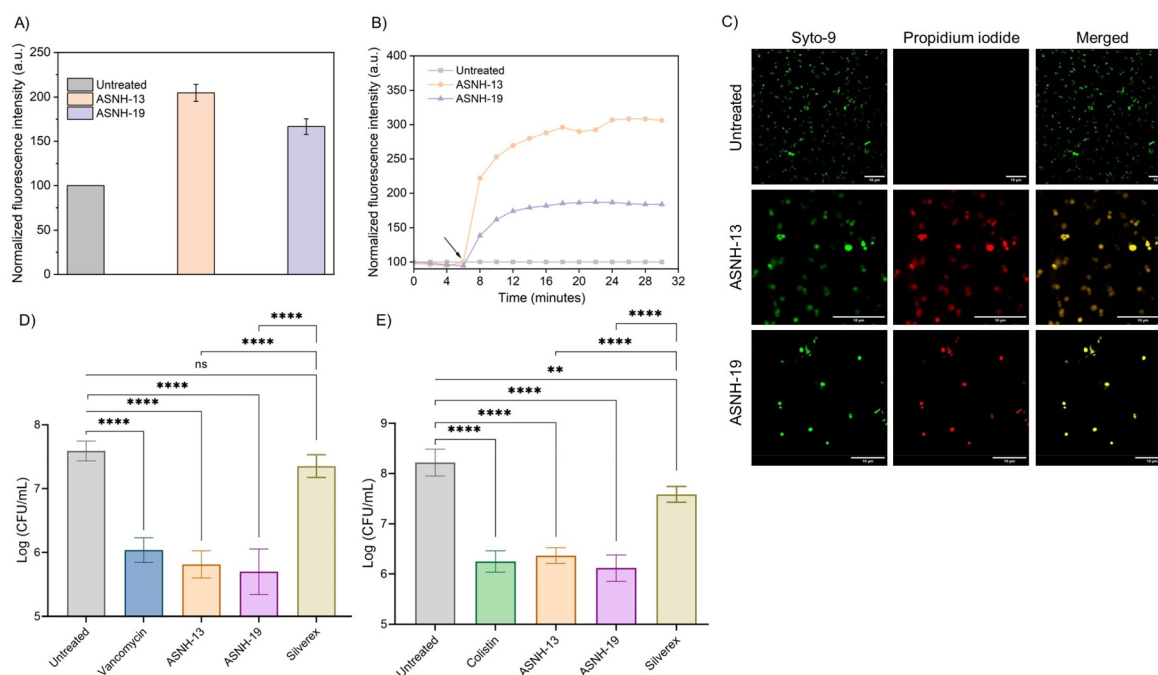
Fig. 4 Multifaceted bactericidal mechanism of action exerted by lead hydrogels. (A) Generation of reactive oxygen species (ROS) by the lead hydrogels against MRSA ATCC 33591. (B) Membrane depolarization assay against MRSA ATCC 33591. Arrow denotes the time of hydrogel addition. (C) Live/dead assay performed against MRSA ATCC 33591. Scale bar is 10 μm. Biofilm disruption activity of the optimized hydrogels against mature biofilms of (D) MRSA ATCC 33591 and (E) *P. aeruginosa* R590. Vancomycin (32 μg mL^{-1}) and colistin (16 μg mL^{-1}) were used as antibiotic controls, respectively. Commercially available colloidal silver-based ointment: Silverex™ (150 mg mL^{-1}) was used as for comparison. Silverex™ contains 0.2% w/w silver nitrate. One-way ANOVA, followed by a Dunnett's multiple comparison test was used for statistical significance, *significantly different from the untreated control, *$p < 0.05$; **$p < 0.01$; ***$p < 0.001$ and ****$p < 0.0001$.

As a result, the fluorescence intensity decreases due to self-quenching within the microbial cells.[61] When membrane-active agents disrupt the membrane potential, they facilitate the release of the dye from the intracellular to the extracellular environment. This leads to a gradual increase in fluorescence intensity over time. In the present study, treatment with hydrogels resulted in a significant and time-dependent enhancement of fluorescence intensity (Fig. 4B), suggesting a pronounced depolarization of the bacterial transmembrane potential. Notably, a stronger effect was observed upon treatment with composite hydrogels containing AgNPs, attributed to its superior antibacterial activity. These findings indicate that the hydrogels effectively depolarize the membrane potential and subsequently kill the microbes.

Membrane permeabilizing ability. The membrane-disruption ability of the hydrogels was further proved through live/dead assay using Syto-9 and PI (propidium iodide) (Fig. 4C). MRSA cells were incubated with the hydrogels for 4 hours, followed by simultaneous staining with Syto-9 (green emission) and PI (red emission). Syto-9 is a membrane-permeable dye that stains both live and compromised bacteria, whereas PI is cell-impermeable and selectively stains dead or membrane-compromised bacteria.[62] In the untreated control group of MRSA, no red cells were observed in the microscopic image, indicating the presence of live bacteria with intact membrane integrity. However, upon treatment with the hydrogels, MRSA cells were stained by both Syto-9 and PI, indicating the presence of dead bacteria with compromised membrane integrity (Fig. 4C). These results provide further evidence of the membrane-disruptive activity of the hydrogels, leading to bacterial cell death.

This finding provides further confirmation of the mechanism of action of hydrogels as agents that interact with bacterial membranes and disrupt them. The live/dead staining results, in conjunction with previous findings, support the notion that the hydrogels exert their antibacterial activity by acting on bacterial membranes.

2.5 Nanocomposite hydrogels eradicate established biofilms with comparable potency to last-resort antibiotics

Microbial biofilms are multicellular structures made up of a self-produced extracellular matrix, acting as a diffusion barrier to antimicrobial agents and harboring predominantly dormant or metabolically inactive bacterial cells.[7,8] As a result, biofilm-associated microbes exhibit significantly higher resistance to antimicrobials compared to their planktonic counterparts. Therefore, we evaluated the anti-biofilm properties of the optimized hydrogels against mature biofilms of MRSA and *P. aeruginosa* through counting bacterial cell viability (Fig. 4D and E). The hydrogels exhibited substantial reduction in bacterial burden. Against MRSA biofilms, they showed ~2 log (~99%) reduction in the bacterial cell viability (Fig. 4D). On the other hand, against *P. aeruginosa* biofilms, they demonstrated superior activity and reduced bacterial burden by >2.5 log (>99%) (Fig. 4E). The last resort antibiotics vancomycin (for Gram-positive bacteria) and colistin (for Gram-negative

bacteria) showed similar levels of anti-biofilm activity and reduced the biofilm bacterial count by ~1.5–2 log. In contrast, the commercially available silver-based ointment Silverex™ (consisting of silver nitrate (0.2% w/w), 100 times more concentrated than the ASNH-13 hydrogel and 5 times more than the ASNH-19 hydrogel) was completely ineffective against biofilms of both the tested pathogens (Fig. 4D and E).

2.6 Nanocomposite hydrogels displayed potent antifungal activity and disrupted fungal biofilms

In addition to the bacterial infection, fungal colonization is one of the major challenges in the case of wound injuries.[9,63,64] Considering the high pathogenicity of *C. albicans* infections, the World Health Organization (WHO) has classified it as a 'critical priority' in the fungal priority pathogen list since 2022.[63] Therefore, the antifungal activity of the optimal hydrogels, ASNH-13 and ASNH-19, was investigated against fluconazole resistant clinical isolates of *Candida albicans* (*C. albicans* AB226 and *C. albicans* AB399). Against these fungal strains, the hydrogels demonstrated complete killing with >5 log reduction within 6 h of incubation (Fig. S5A). The control hydrogel (ASH) devoid of metal nanoparticles did not show any antifungal activity. After that, the rapid mechanism of antifungal activity was investigated through live/dead assay. Similar to MRSA, against the fungal strain *C. albicans* AB226, the hydrogels exhibited a membrane disrupting nature proved through red fluorescence in the PI channel (Fig. S5B). Collectively, the optimal hydrogels demonstrated broad spectrum antimicrobial activity against both drug-sensitive and drug-resistant bacteria as well as fungi without causing any toxicity towards human red blood cells.

Similar to the bacterial biofilms, fungal biofilms also show recalcitrance to the conventional anti-fungal agents.[63,64] *C. albicans* cells, in particular, can penetrate the epidermis and dermis, forming dense biofilms in deep cutaneous tissue.[65,66] Therefore, the fungal biofilm disruption ability of the hydrogels was also tested through a fungal cell titer. The hydrogel treatment caused ~1.5 log (>95%) reduction in the fungal cell counts as well (Fig. 5A). The last resort antifungal drug amphotericin B displayed superior activity, causing >3 log reduction in the cell viability. However, the cytotoxicity of amphotericin B is a major problem limiting its widespread use. Similar to the bacterial biofilms, the colloidal silver-based ointment Silverex™ showed minimal reduction in the case of fungal biofilms as well. Overall, these findings underscore the potency of the hydrogels in treating complicated infections caused by bacterial and fungal biofilms.

2.7 Nanocomposite hydrogels outperform last-resort antibiotics and commercial ointments in eradicating polymicrobial biofilms

In addition to forming single species biofilms, *C. albicans* is frequently found within polymicrobial communities in chronic wound infections, dental plaques, cystic fibrosis, gastrointestinal tract infections, *etc.*[9–11] The cross-kingdom interactions in polymicrobial biofilms enhance virulence, increase drug resis-
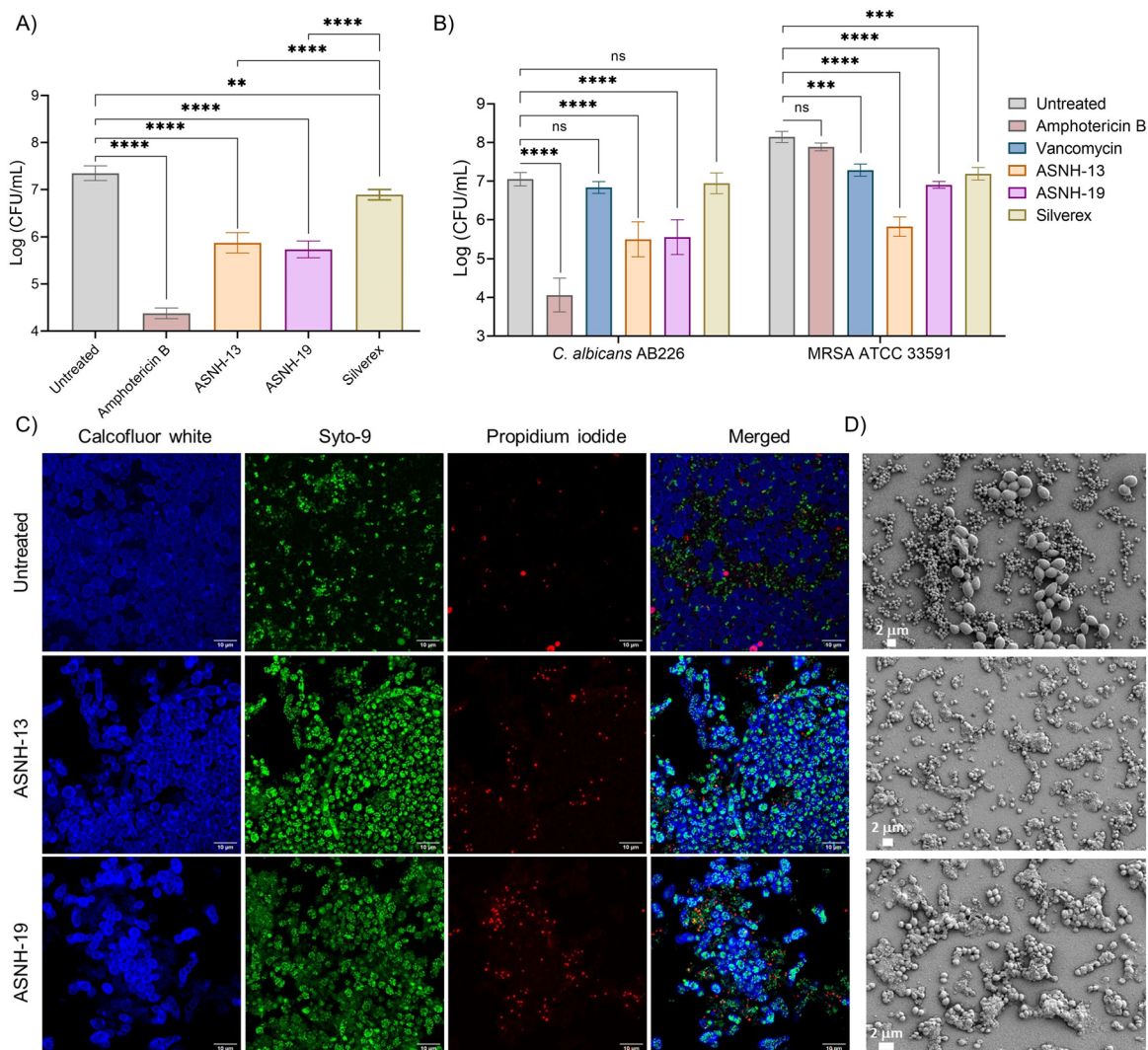
Fig. 5 (A) Biofilm disruption activity of the optimized hydrogels against mature biofilms of *C. albicans* AB226. (B) Biofilm disruption activity of the optimized hydrogels against mixed species biofilms composed of MRSA ATCC 335591 and *C. albicans* AB226. Amphotericin B (5 μg mL^{-1}) and vancomycin (32 μg mL^{-1}) were used as antibiotic controls. Commercially available colloidal silver-based ointment: Silverex™ (150 mg mL^{-1}) was used for comparison. Silverex™ contains 0.2% w/w silver nitrate. One-way ANOVA, followed by a Dunnett's multiple comparison test was used for statistical significance, *significantly different from the untreated control, *$p < 0.05$; **$p < 0.01$; ***$p < 0.001$ and ****$p < 0.0001$. (C) Confocal microscopy images of the polymicrobial biofilm formed by MRSA ATCC33591 and *C. albicans* AB226 through simultaneous staining of Calcofluor white, Syto-9 and PI staining. Scale bar is 10 μm. (D) FESEM images of the polymicrobial biofilm (top to bottom): untreated control, ASNH-13 and ASNH-19 hydrogel treatment. Scale bar is 2 μm.

tance, and exacerbate disease severity compared to those with mono-microbial biofilms. Among these interactions, the synergistic relationship between *C. albicans* and *S. aureus* has been extensively studied, revealing increased biofilm formation and lethality. The dual antimicrobial and biofilm disruption properties of our lead hydrogels prompted us to evaluate their efficacy against polymicrobial biofilms. Treatment with hydrogels resulted in significant reduction of both fungal and bacterial burden (Fig. 5B). In the case of fungi, both the hydrogels ASNH-13 and ASNH-19 displayed ~1.5 log reduction, whereas amphotericin B displayed ~3 log reduction at its high therapeutic concentration (>20 × MIC). However, amphotericin B was unable to reduce the bacterial count in the biofilm.

Interestingly, the lead hydrogels successfully brought down the MRSA burden as well. ASNH-19 displayed ~1.5 log reduction, whereas ASNH-13 exhibited >2 log reduction in the bacterial titer (Fig. 5B). The last resort antibiotic against Gram-positive bacteria, vancomycin, was totally inefficient against both bacteria and fungi even at a high concentration of 32 μg mL^{-1}. None of the antibiotics used in this study were able to kill simultaneously both the organisms, proving the complexity of the polymicrobial biofilms (Fig. 5B). Additionally, the commercially available colloidal silver-based formulation (Silverex™) exhibited minimal efficacy against the polymicrobial biofilm, further emphasizing the superior performance of our hydrogel formulations (Fig. 5B). Unlike conventional antibiotics and

silver-based formulations, which were unable to target both organisms simultaneously, the lead hydrogels effectively reduced the microbial burden of both *C. albicans* and MRSA, highlighting their potential to address the complexity of polymicrobial biofilms.

The disruption of polymicrobial biofilms was further visualized through confocal microscopy of the mixed biofilm, which was performed by staining with Calcofluor white, Syto-9 and PI. Calcofluor white selectively stains chitin in the fungal cell wall and produces strong blue fluorescence (Fig. 5C). Syto-9 stains both live and dead microbial cells and produces green fluorescence. On the other hand, PI can only enter membrane compromised cells and produce red fluorescence. The fungal

cells appeared bigger than the bacterial cells because of their larger size. In the control biofilm, both bacterial and fungal species showed good co-habitation together. The antifungal drug, amphotericin B, could only kill the fungal cells as strong red fluorescence was observed merging with blue (fungal) fluorescent cells. However, there were a huge number of viable bacterial cells in the biofilm (Fig. S6). On the other hand, ASNH-13 and ASNH-19 hydrogel treatment significantly killed both the cells within the biofilm as red fluorescence was observed from both bacteria and fungi. Similarly, FESEM of the polymicrobial biofilm was also performed. Untreated biofilms showed co-existence of both the microbes in clusters, where the smaller bacterial cells were found sticking to the
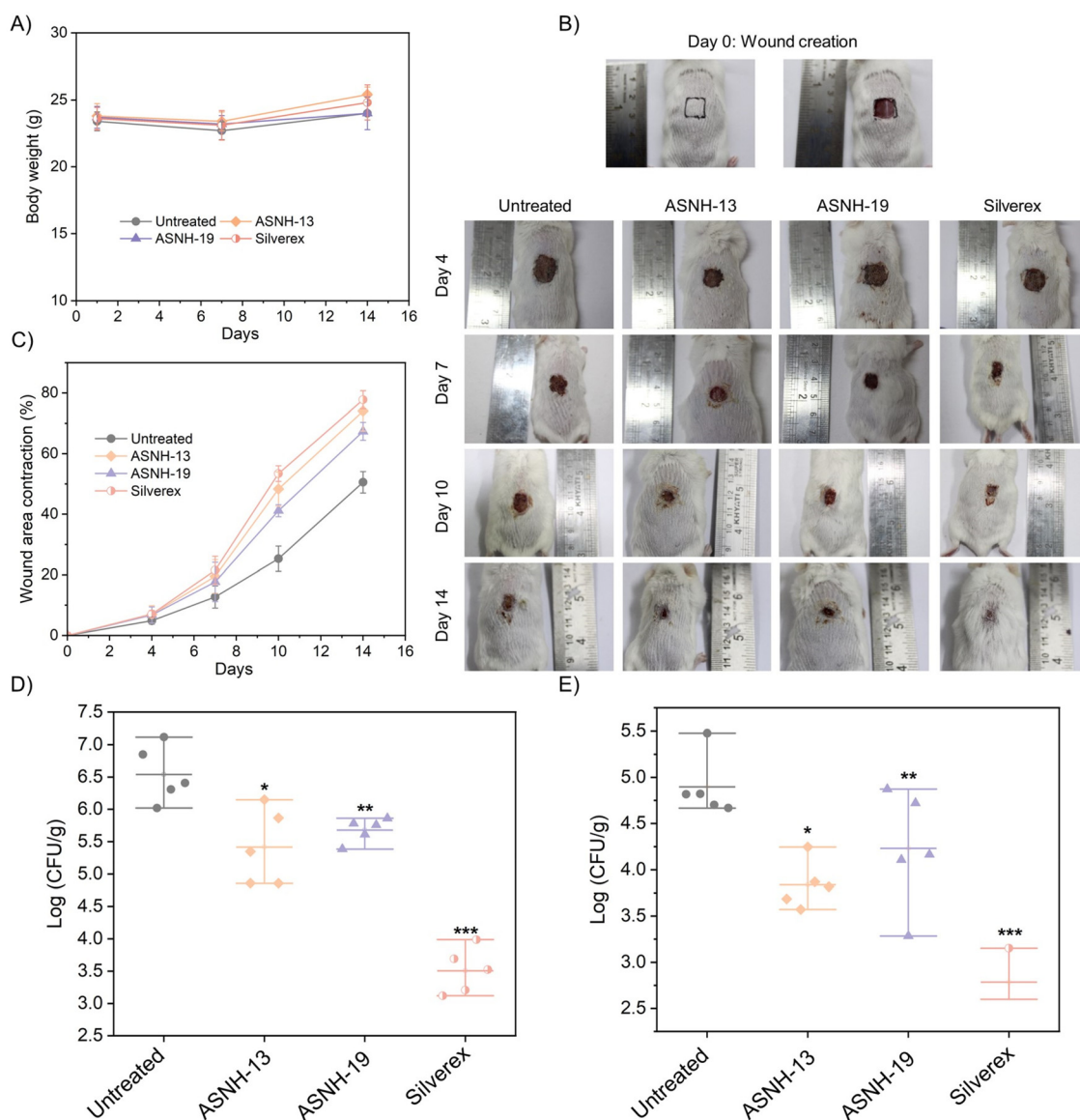
Fig. 6 Infected wound healing ability of the optimized hydrogels. (A) Changes in the body weight upon application of the hydrogels. (B) Representative images of the wound at different days. (C) Percentage of wound area contraction at different days. Bacterial burden in the infected tissues after (D) 7 days and (E) 14 days. One-way ANOVA, followed by a Dunnett's multiple comparison test was used for statistical significance, *significantly different from the untreated control, *$p < 0.05$; **$p < 0.01$ and ***$p < 0.0001$.

bigger fungal cells (Fig. 5D). Both the cells showed intact morphology. However, both the hydrogel treatment disrupted the biofilm, compromising their cell membrane structure stemming from their membrane targeting mode of action (Fig. 5D). The ASNH-13 hydrogel with AgNPs demonstrated superior efficacy accompanied by the presence of abundant cellular debris. This result demonstrated the unique properties of this class of metallohydrogels to tackle polymicrobial biofilm associated infections.

2.8 Nanocomposite hydrogels exhibited potent *in vivo* biocompatibility

To further strengthen the applicability of the hydrogels, biocompatibility was investigated in a mouse model. For that the mouse skin was shaved at the dorsal area and hydrogels were applied and inflammatory responses were observed throughout 7 days (Fig. S7). It was observed visually that the hydrogel treatment did not trigger any inflammatory responses like skin redness, irritation, convulsions, tremors, salivation, *etc.* (Fig. S7). After 7 days of treatment, histopathological analysis

of the skin tissues was performed (Fig. S7). ASNH-13 and ASNH-19 treated skin tissue showed the normal architecture of the epidermis lined by stratified squamous epithelial cells and a keratin layer without the infiltration of inflammatory cells, similar to the untreated control (Fig. S7). The dermis layer showed the presence of sweat and sebaceous gland (SG) and hair follicles (HF). Adipose tissue (AT) containing fat cells with nuclei placed at the periphery was also observed. Overall, the hydrogels showed potent biocompatibility both *in vitro* and *in vivo*, proving their immense potential to be used as a wound dressing material.

2.9 Nanocomposite hydrogels accelerate wound healing and effectively treat MRSA infections in mice

After detailed investigation of *in vitro* antimicrobial activity, the *in vivo* efficacy of the hydrogels was assessed in an excision wound infection model infected with MRSA (ATCC 43300). Mice were divided into four groups and the hydrogels were topically applied daily. The efficacy parameters were evaluated in terms of percentage wound contraction, bacterial load in
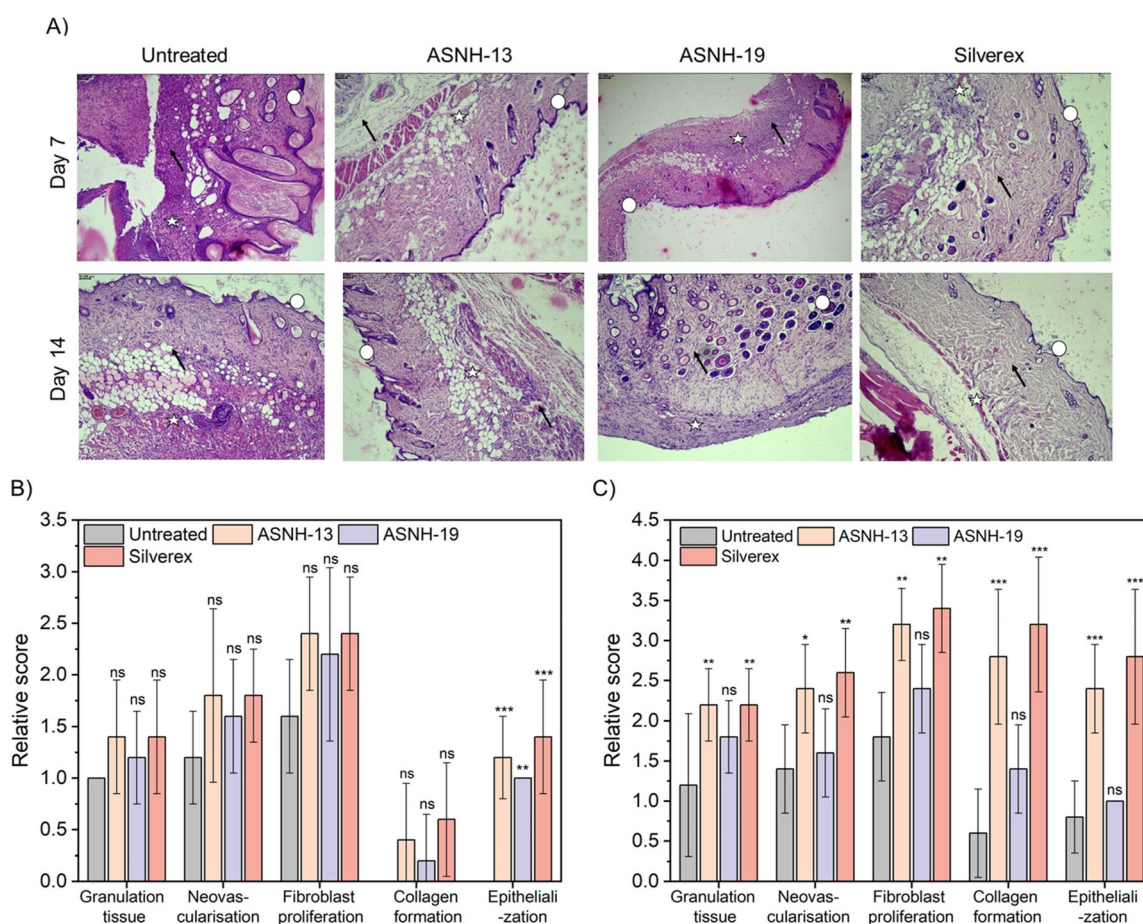
Fig. 7 (A) Histopathological analysis of the wound tissues after 7 and 14 days. 'Arrow' represents collagen deposition, 'star' denotes neovascularization and 'circle' indicates epithelization. Histological scores of different parameters, namely the presence of granulation tissue, neovascularization, fibroblast proliferation, collagen formation, and epithelialization in the infected tissues at (B) day 7 and (C) day 14. One-way ANOVA, followed by a Dunnett's multiple comparison test was used for statistical significance, *significantly different from the untreated control, ns = not significant, $*p < 0.05$; $**p < 0.01$ and $***p < 0.0001$.

the infected tissues and histopathology of skin for neovascularization, granulation tissue, epithelialization and collagen formation. All animals were apparently normal throughout the experiment. There was no significant difference between loss or gain in body weight throughout the 14 days (Fig. 6A). Untreated group mice showed percentage wound contraction of 4.88%, 12.74%, 25.32%, and 50.54% on days 4, 7, 10 and 14, respectively (Fig. 6B and C). ASNH-13 exhibited percentage wound contraction of 6.96% ($p > 0.05$), 19.49% ($p > 0.05$), 48.30% ($p < 0.001$) and 74.06% ($p < 0.001$) on days 4, 7, 10 and 14, respectively (Fig. 6B and C). Daily application of ASNH-19 for 14 days showed accelerated wound contraction of 6.78% ($p > 0.05$), 17.67% ($p > 0.05$), 41.16% ($p < 0.001$) and 67.36% ($p < 0.001$) on days 4, 7, 10 and 14, respectively (Fig. 6B and C). The commercially available hydrogel Silverex™ ionic gel demonstrated percentage wound contraction of 7.07% ($p < 0.001$), 21.51% ($p < 0.001$), 53.41% ($p < 0.001$) and 77.78% ($p < 0.001$) on days 4, 7, 10 and 14, respectively (Fig. 6B and C). All treatment groups exhibited a significant reduction ($p < 0.05$) in bacterial load on days 7 and 14 (Fig. 6D and E). In the case of the untreated control, the bacterial count increased to 6.54 ± 0.44 CFU g^{-1} on day 7. In contrast, treatment with a hydrogel consisting of AuNPs (ASNH-19) reduced the bacterial count to 5.68 ± 0.19 (~90% reduction; $p < 0.05$) on day 7 (Fig. 6D). On the other hand, the hydrogel with AgNPs (ASNH-13) exhibited superior efficiency with ~94% reduction in bacterial viability at day 7 ($p < 0.01$) and >90% reduction at day 14 (Fig. 6D and E). The commercial ointment Silverex™ demonstrated ~3 log and ~2 log reduction in bacterial burden at day 7 and day 14. The higher percentage of colloidal silver accounts for its superior activity.

The histological sections demonstrated that the healing process observed macroscopically was consistent with the microscopic evaluation (Fig. 7A). Histopathological analysis of the skin tissues from the untreated control group on day 7 showed severe multifocal inflammation. Microscopic examination of the skin on day 7 from the treatment groups (ASNH-13, ASNH-19 and Silverex™) with MRSA infection showed a substantial reduction in the inflammatory response and a significant increase in epithelialization ($p < 0.0001$). However, the relative scoring for collagen formation, fibroblast proliferation, neovascularization and granulation tissue formation were not significant ($p > 0.05$), when compared with the untreated control (Fig. 7B). On the other hand, skin tissues on day 14 from the treatment groups (ASNH-13 and Silverex™) showed a significant increase in granulation tissue formation ($p < 0.01$), neovascularization ($p < 0.05$ & $p < 0.01$), fibroblast proliferation ($p < 0.01$), collagen formation ($p < 0.0001$), and epithelialization ($p < 0.0001$), respectively, when compared with the untreated control (Fig. 7C). Nevertheless, the relative scores of these parameters in the case of ASNH-19 did not significantly improve. Despite all the treatment groups showing diminished inflammation at the infected tissues the untreated control group still showed moderate multifocal inflammation. The study demonstrates that topical treatment with hydrogel formulations containing AuNPs and AgNPs significantly

enhances wound healing efficacy by days 10 and 14. The commercially available hydrogel significantly improved wound healing by day 7, with continued efficacy on days 10 and 14. However, the potential toxicity of Silverex™ and its limited efficacy to counter microbial biofilms manifests the superior efficiency of our formulations. The histological analysis, showing a significant increase in fibroblast proliferation, collagen formation, and epithelialization in the treatment groups by day 14, strengthens these observations.

3. Conclusions

This study highlights the development of peptide-based metal nanocomposite hydrogels as a versatile and transformative solution for tackling the pressing challenge of drug-resistant infections and polymicrobial biofilm-associated complications. Utilizing a sunlight-driven, *in-aqueous* and *in situ* synthesis approach, these hydrogels circumvent the need for toxic reducing agents, ensuring biocompatibility while demonstrating potent, broad-spectrum antimicrobial activity against multidrug-resistant bacteria and fungi. The dual efficacy of these metallohydrogels in disrupting polymicrobial biofilms, including eradicating single species fungal and bacterial communities, underscores their superiority over conventional antimicrobials and commercial formulations. Furthermore, their remarkable ability to accelerate wound healing through enhanced tissue regeneration and reduction of microbial burden further substantiates their therapeutic potential. The simplicity, scalability, and economic viability of their fabrication, coupled with robust antimicrobial and wound-healing properties, make these nanocomposite hydrogels a promising candidate as a next generation wound dressing biomaterial.

4. Experimental section

4.1 Reagents and materials

N-Fluorenylmethoxycarbonyl-diphenylalanine (Fmoc-FF) was purchased from LifeTein, USA, *N*-fluorenylmethoxycarbonyl-arginine–glycine–aspartic acid (Fmoc-RGD) was purchased from SynPeptide Shanghai, China, and hydrolyzed collagen (collagen type I (liquid) from rat tail CAS: 9007-34-5) was purchased from Guinama, Spain. All gelators were used without further purification. Gold(III) chloride trihydrate (HAuCl$_4$·3H$_2$O) was purchased from Sigma-Aldrich and silver nitrate (AgNO$_3$) was purchased from Scharlau. *S. epidermidis* MTCC 3615, *P. aeruginosa* MTCC424 and MRSA ATCC 33591 were purchased from MTCC (Chandigarh, India) and ATCC (Rockville, MD, USA) respectively. *A. baumannii* R674, *E. coli* R3336, *K. pneumoniae* R3934 and *P. aeruginosa* R590 were obtained from the National Institute of Mental Health and Neurosciences (NIMHANS), Bangalore, India. Fungal strains (*C. albicans* AB226 and *C. albicans* AB399) were obtained from Anthem Biosciences, Bangalore, India. Nutrient media and agar, YPD media and agar to grow the bacterial cultures were

bought from HIMEDIA, India. A Tecan infinite pro series M200 microplate reader was used to measure the optical density (OD) and fluorescence intensity.

4.2 Preparation of basic solutions of peptides

Fmoc-FF and Fmoc-RGD were weighed separately into a vial and deionized water was added to obtain a final concentration of 20 mM stock solutions. The suspension was sonicated (in a HSt Powersonic 405-ultrasonic bath) for at least 2 hours. The Fmoc-RGD final solution was obtained without the addition of NaOH. Then, to obtain the final Fmoc-FF solution a NaOH solution (0.5 M) was added dropwise until a clear solution (pH = 10.7) was obtained. The pH was measured using a HACH Sension PH 3 pH meter. The pH meter was calibrated using pH 4, pH 7 and pH 10 buffer solutions.

4.3 Formation of composite supramolecular hydrogels

To obtain the composite hydrogels formed with Fmoc-FF, collagen and Fmoc-RGD, they were mixed following this sequence with a ratio of 3.5 : 5 : 1.5 and for a final concentration of 6.95 mg mL^{-1} of the organic materials.

4.4 Formation of nanocomposite hydrogels

To obtain metallogels with Fmoc-FF, metallic salts of gold and silver were added to the basic solution of the peptide, inducing gelation (for the concentrations of 1.18–2.76 mg mL^{-1} for Au^{3+} and 0.51–1.19 mg mL^{-1} for Ag^{+}, and for the less concentrated sample, hydrogels are not obtained). The final concentration of Fmoc-FF in all samples was 10 mM and for salts, a screening was carried out with the following concentrations:

Cations		
Metal	[Metallic salt] (mg mL^{-1})	[Metallic salt] (mM)
HAuCl$_4$·3H$_2$O	0.04, 0.20, 0.39, 1.18, 1.97, 2.76	0.1, 0.5, 1, 3, 5, 7
AgNO$_3$	0.02, 0.08, 0.17, 0.51, 0.85, 1.19	0.1, 0.5, 1, 3, 5, 7

To obtain metallogels with the composite formed with Fmoc-FF, Fmoc-RGD and collagen, the sequence of mixture was Fmoc-FF, collagen, metallic salt of gold and silver and, finally, Fmoc-RGD, inducing gelation for all concentrations due to the drop in the pH values because of the addition of Fmoc-RGD.

4.5 Rheological characterization of hydrogels

Mechanical properties were characterized under oscillatory shear stress using a Bohlin CS10 controlled-stress rheometer (UK) provided with a plate–plate geometry with 40 mm diameter. We subjected the samples to tests of constant frequency and increasing shear stress amplitude (amplitude sweeps), and then to tests of constant shear stress amplitude (τ_0 = 1 Pa) within the Linear Viscoelastic Region (LVR) and increasing frequency in the range 0.1–10 Hz. From these measurements, we obtained the storage (G') and loss (G'') moduli of the samples as a function of frequency within the LVR (mechanical

spectra). Three different samples were measured to ensure statistical significance of the results. The mean values and standard deviations of each magnitude are provided in this work.

4.6 Transmission electron microscopy

Dried gels were studied with a LIBRA 120 PLUS Carl Zeiss. Hydrogels were vortexed and diluted twice with water. A drop of the fiber suspension obtained was placed on a 300-mesh copper grid and stained with uranyl acetate negative stain. The sample was dried at room temperature for 1 h.

4.7 Environmental scanning electron microscopy

Refrigerated samples of peptide hydrogels were examined by ESEM using a FEI Quanta 400 equipped with a Peltier effect cooling stage.

4.8 Uv-Visible spectrophotometry

UV-Visible spectra were recorded from a diluted sample of the hydrogels containing MNPs in a ratio of 1 : 5 in MilliQ water. The spectra were scanned over the range between 350 nm to 700 nm. Absorption measurements were performed in an Olis DSM172 spectrophotometer using a 1.0 cm path-length quartz cell.

4.9 Fourier transform infra-red (FT-IR) spectroscopy

Spectra were recorded using a PerkinElmer Two FT-IR ATR spectrometer. The hydrogels were dried at room temperature to obtain the xerogels and then they were compressed onto the diamond crystal. All spectra were scanned over the range between 4000 and 450 cm^{-1}.

4.10 Equilibrium water content (EWC)[67]

Hydrogels were weighed using an analytical weighing balance (Sartorius® BSA224S-CW) with an accuracy of 10^{-4} g in fully hydrated and dried states. Complete drying was achieved by freeze-drying at 0.1 bar for 6.5 hours. The EWC was calculated using the gravimetric method in replicates of 3, following the equation below:

$$\text{Equilibrium water content}\,(\%) = \frac{W_s - W_d}{W_s} \times 100$$

where W_s = weight of the hydrogel in the fully hydrated state and W_d = weight of the hydrogel when completely dried.

Water retention capacity.[67] The water retention capacity (WR$_t$) of the gels was calculated as a function of time using the equation below:

$$\text{WR}_t = \frac{W_p - W_d}{W_s - W_d} \times 100$$

where W_p is the weight of the hydrogel at various exposure times and W_d is the wight in the dry state. The exposure area of gels to the external environment at 37 °C/70 ± 5% RH was ~60 mm^2. The analysis was carried out over 8 hours in replicates of 3.

Swelling ratio.[67] In order to determine the swelling ratio, the hydrogels were completely dried using a Labconco® lyophilizer. The gels were weighed, and immersed in 1× PBS at 37 °C to visu-

alize swelling under physiological conditions. At specific time points, the gel was centrifuged at 10 000 rpm for 2 min at 25 °C. The excess PBS was removed by pipetting, blotted with a filter paper and the gels were weighed to obtain the wet weight. The swelling ratio was calculated and plotted against time:

$$\text{Swelling ratio} \ (q) = \frac{W_t - W_d}{W_d}$$

where W_t is the weight of the hydrogel at various exposure times in water and W_d is the weight in the dry state.

Antibacterial activity of the hydrogels.[67] Mid-log phase bacterial culture ($\sim 10^8$ CFU ml^{-1}) was diluted to $\sim 10^6$ CFU mL^{-1} in 1× PBS. 100 mL of the diluted bacterial solution was mixed with a hydrogel (100 mL) and incubated for next 12 h. After that the solution was serially diluted in saline, dropcast on a nutrient agar plate and incubated for another 18 h. After 18 h, the viable cells were counted. The protocol was used following our JNCASR Institutional Biosafety Committee (IBSC) guidelines (JNC/IBSC/2024/JH/EXTN/C-28). The experiment was performed in triplicate and the antibacterial activity was reported by considering the average bacterial count with standard deviation.

Hemolytic activity of the hydrogels.[67] The hemolytic activity experiment was performed in accordance with the guidelines of Indian Council of Medical Research (ICMR), and it was approved by the JNCASR Institutional Ethical Committee (IEC) (JNC/IEC/M5-2024/JH-003). Informed consent was obtained from the healthy human participants of this study following our institutional ethical committee guideline. Freshly collected human blood (heparinized) was then centrifuged and the supernatant was rejected to collect the human red blood cells (hRBCs). Later, the collected hRBCs (5 vol%) were slowly suspended using 1× PBS (pH = 7.4). Next, 100 µL of this suspension was added to the hydrogel (100 µL) in a 96-well plate, and the plate was allowed to incubate at 37 °C for 1 h. After that, centrifugation at 3500 rpm was performed for 5 min, and the supernatant (100 µL) was then transferred to another 96-well plate to record the absorbance at 540 nm by using a microplate reader. In this study, the same volume of 1× PBS without a hydrogel was used as a negative control, whereas the same volume of Triton X- (1 vol% solution in 1× PBS) was used as a positive control. The percentage of hemolysis was determined by using the following formula: $(A_{\text{treated}} - A_{\text{untreated}})/(A_{\text{TX-treated}} - A_{\text{untreated}}) \times 100$, where A_{treated} corresponds to the absorbance of the hydrogel treated well, $A_{\text{untreated}}$ stands for the absorbance of the negative controls (without a hydrogel), and $A_{\text{TX-treated}}$ is the absorbance of the Triton X-treated well. The experiment was performed in triplicate and the hemolysis was determined by considering the average of triplicate O.D. measurements.

Antifungal activity.[62] Following our standard lab protocol, fungal strains were grown on YPD agar plates streaked from frozen stock (−80 °C) supplemented with glycerol and incubated for 28 °C for 24 h. The protocol was used following JNCASR Institutional Biosafety Committee (IBSC) Guidelines (JNC/IBSC/2024/JH/EXTN/C-28). A single fungal colony was

inoculated in 3 mL YPD medium for 10 h at 28 °C to grow mid-log phase fungi ($\sim 10^8$ CFU mL^{-1}). This mid-log phase culture was then diluted to $\sim 10^5$ CFU mL^{-1} in 1× PBS. 100 µL of the diluted bacterial solution was mixed with the hydrogel (100 µL) and incubated for the next 6 h. The experiment was performed in triplicate and the activity will be reported by considering the average fungal count with standard deviation.

ROS generation assay.[68] The assay was performed using 2′,7′-dichlorofluorescein diacetate (DCFH-DA). In summary, 100 µL of hydrogels were incubated with 1 mL of 10^8 CFU mL^{-1} MRSA cells. After that, the bacterial suspension from each replicate was collected in a 1.5 mL microtube, and the biocide that had been released into the suspension was removed by centrifuging the mixture for 5 min at 3500 rpm. Following this, 1 mL of 1× PBS was used to resuspend the bacterial pellet, and 10 µM DCFH-DA dye was added to the mixture. After 45 min of incubation period, fluorescence was measured with excitation and emission at 485 nm and 530 nm, respectively.

Membrane depolarisation assay.[69] Briefly, the planktonic bacterial cells of MRSA ATCC 33591 ($\sim 10^8$ CFU mL^{-1}) were centrifuged at 3500 rpm for 5 min and pelleted down. The supernatant medium was discarded, and the cells were washed with 5 mM HEPES buffer (pH = 7.4), and subsequently, resuspended in the solution containing a 1 : 1 : 1 ratio of 5 mM glucose, 5 mM HEPES buffer and 100 mM KCl solution complemented with 250 µM of EDTA solution. Next, DiSC$_3$ (5) (3,3′-dipropylthiadicarbocyanine iodide) dye was mixed in bacterial suspension to attain the final concentration of 2 µM. The dye containing bacterial solution was kept for incubation in the dark for 60 min. Then, 190 µL of the dye containing bacterial suspension was placed in a black and clear bottom 96-well plate and subsequently, the fluorescence intensity of the dye was measured. Next, 10 µL hydrogel was mixed and the fluorescence intensity was measured for the next 22 min. As a negative control, 10 µL of sterile water was added.

Live/dead assay.[70] In brief 1 mL of bacterial/fungal cells was pelleted down by centrifuging at 3500 rpm for 5 minutes. The medium was discarded, and the cells were washed with 0.9% saline followed by resuspension in 1 mL saline. Then 100 µL of hydrogels was added to this suspension and allowed to incubate for 2 h at 37 °C. Afterwards, the solution was centrifuged, and the cells were re-suspended in saline followed by the addition of Syto-9 and PI to obtain a final concentration of 3 µM and 15 µM, respectively. This dye containing solution was incubated in the dark for 15 min. The solution was centrifuged and washed with saline to remove the excess dye. Next 5 µL of this solution was subjected to fluorescence microscopy and the images were captured using a Leica DM2500 microscope. For Syto-9 a band pass filter of 450–490 nm wavelength and for propidium iodide a filter of 515–560 nm wavelength were used.

Bacterial biofilm disruption assay.[71] Briefly, the biofilms of MRSA and *P. aeruginosa* were grown in sterile cover slips by incubating them in mid log-phase bacterial solution (10^5 CFU mL^{-1}) in nutrient broth supplemented with 1% glucose and

1% NaCl for 1 and 3 days, respectively. Once the mature biofilms were formed, they were washed with 1× PBS to remove the unadhered bacteria. Then the biofilms were treated with 100 µL of hydrogels and incubated for 24 h. After 24 h, the cover slips were treated with trypsin-EDTA solution in saline (1:10) and incubated for 10 minutes. After that, the biofilms were scratched out and the solutions were serially 10-fold diluted. 20 µL of these diluted solutions were spot plated on a nutrient agar plate and viable cells were quantified after 18 h of incubation. The experiment was performed in triplicate and the activity was reported by considering the average bacterial count with standard deviation.

Disruption of polymicrobial biofilms.[72] Activity against polymicrobial biofilms was observed against *C. albicans* and MRSA. Briefly, the individual culture of mid-log phase fungi (*C. albicans* AB226) and bacteria (MRSA ATCC33591) was diluted to ~10^5 CFU mL^{-1} and ~10^6 CFU mL^{-1} in potato dextrose broth (PDB) and nutrient broth (NB) media (1:1). Then 2 mL of fungal solution and 200 µL of bacterial solution were added to the wells of a 6 well plate containing a sterilized glass coverslip and they were incubated at 37 °C for 24 h. Afterwards, the coverslips were washed in saline and treated with 200 µL hydrogel at different concentrations and allowed to incubate at 37 °C for 24 h. The biofilms were then trypsinized using 2 mL of trypsin-EDTA solution in saline (1:10) and incubated for 15 min. Next these coverslips were carefully scratched, and the cell suspension was then serially 10-fold diluted in saline and 20 µL of the diluted solutions was spot plated on amphotericin B (100 µg mL^{-1}) containing a nutrient agar plate for MRSA and vancomycin (150 µg mL^{-1}) containing YPD agar plates for *C. albicans.* These plates were then incubated for 24 h at 37 °C for bacteria and 48 h at 30 °C for fungi.

Confocal microscopy. For confocal microscopy, the biofilms were stained with Calcofluor white, Syto-9 and PI with final concentrations of 0.8 mg mL^{-1}, 60 µM and 15 µM in saline. Images were captured with the help of a Zeiss 510 Meta confocal laser-scanning microscope. ImageJ was used to process the images.

Scanning electron microscopy. The coverslips (both untreated and treated) were washed with 1× PBS and transferred to a new 6-well plate. After that they were fixed with 2.5% (v/v) glutaraldehyde solution for 60 min. Subsequently, they were dehydrated through a series of ethanol gradients from 30% to 100%. After that, they were air-dried and gold coated before SEM imaging.

***In vivo* biocompatibility.**[73] All animal procedures were performed in accordance with the guidelines for care and use of laboratory animals of JNCASR and approved by the JNCASR Institutional Animal Ethical Committee (IAEC) guidelines (201/Go/ReBi/S/2000/CPCSEA). *In vivo* biocompatibility of the hydrogels was evaluated by applying them on mouse skin for 7days. In brief, male BALB/c mice (age 6–8 weeks) were used for the experiments. Before the experiment, the dorsal area of the mice was shaved clearly. Then 150 µL of the hydrogels were applied topically. The saline treatment group was considered the untreated control. After 7 days, the dermal tissues were isolated and stored in 10% neutral buffer formalin (NBF) solution to perform the histopathological analysis.

***In vivo* wound infection studies.**[74] The *in vivo* infected wound healing ability of the hydrogels was investigated in collaboration with TheraIndx Lifesciences. A day prior to infection, Day-1, an aliquot of the glycerol stock MRSA (ATCC 43300) was thawed and inoculated into fresh Casein Soybean Digest (CSD) broth and incubated overnight in a shaking incubator at 37 °C. On the day of infection, the overnight grown culture was adjusted to ~10^8 CFU ml^{-1} in CSD broth and used for infection. The inoculum was serially diluted ten-fold in sterile CSD broth and 0.05 mL of six dilutions were plated on CSD agar plates and placed in an incubator at 37 °C, to check the bacterial density of the inoculum.

One day before wound creation the dorsal skin of the animals was shaved using a pet trimmer. The animals were anesthetized by intraperitoneal injection of ketamine (70 mg kg^{-1}) + xylazine (10 mg kg^{-1}) cocktails. The depth of anesthesia was checked by tail pinch. A wound of about 1 cm × 1 cm was made on the depilated dorsal thoracic region of the animal. Under aseptic conditions, a pre-determined area of 1 cm × 1 cm skin with its full thickness was excised using autoclaved surgical instruments under anesthesia. After excision, 5 mg kg^{-1} of ketoprofen was administered subcutaneously to reduce the pain and stress. Following wound creation, the animals were housed individually with enrichment of species. On the day of wound creation, the wound area was measured by tracing the wound boundaries on a transparent paper. Infections were conducted in a biological safety cabinet, with appropriate personal and respiratory protection. Immediately after excision skin wounding, the mice were inoculated with 50 µl of MRSA (ATCC 43300) (~10^7 CFU ml^{-1}) at the site of skin wound. A gentle shaking/mixing of the inoculum between two animals was followed for uniform distribution, and during the procedure the vial containing the inoculum was placed on ice to minimize *in vitro* multiplication.

Treatment started one hour after infection, and the animals were treated with 150 µL hydrogels or 150 mg Silverex™ on wound topically, daily for 14 days. As mentioned in the experimental design post-treatment, the whole wound was swabbed with a cotton swab for 5 animals from each group on days 1, 3, 5, and 7. On day 7, five animals from each group were terminated and a part of the skin was collected and homogenized in 1 ml saline. On day 14, the remaining five animals from each group were terminated; a part of the skin was collected and homogenized in 1 mL saline. 100 µL of undiluted cell suspension/homogenate or its 100-fold dilutions were plated and incubated on CSD agar plates at 37 °C overnight (16 h) for bacterial enumeration.

Percentage wound contraction. For five animals on days 0, 4, 7, 10 and 14, wounds were measured by following the progressive changes in the wound area metrically, excluding the day of wounding. The size of the wound was traced on a transparent paper, throughout the monitoring period. The tracing was placed on graph paper, from which the wound surface area was estimated. The evaluated surface area was used to calculate the per-

centage of wound contraction, taking the initial size of the wound, 100 mm^2, as 100%, using the following formula:

$$\% \text{ wound contraction} = \frac{\text{initial wound size} - \text{specific day wound size}}{\text{initial wound size}} \times 100$$

On day 7 (5 animals each group) and on day 14 (5 animals each group) animals, after wound measurement, were sacrificed by an overdose of CO_2, and skin samples were collected for bacterial load and histopathological analysis.

Histological analysis. Skin samples collected on the final day were processed and paraffin blocks prepared. The blocks were sectioned to 3 to 5 microns using a rotatory microtome and mounted on clean glass slides. The slides were stained with haematoxylin–eosin (H&E) stain, and sections were assessed with respect to fibroblast proliferation, collagen formation, neovascularization, granulation tissue formation, and epithelialization using a 4-point scale as follows: 0 = none, 1 = rare or minimal, 2 = moderate, 3 = abundant, and 4 = severe or marked. For each specimen, three separate sections were selected randomly for histological evaluation.

Clinical observations:

(a) Body weights: body weights were recorded on day 1 and weekly during the study period.

(b) Clinical signs: the animals were observed for clinical signs, mortality and morbidity once daily during the entire experimental period.

Data analysis. The mean ± SD values for wound sizes, body weights, bacterial load and histopathology scorings were estimated for each group. Statistical analysis was done with the appropriate statistical test using software Graphpad Prism (v 5.0). The significance of differences was reported at a 95% confidence level. HP analysis results were summarized in terms of scores and representative images are shown.

Author contributions

S. M.: conceptualization, experimentation, data analysis, and writing original draft; M. N.-M.: conceptualization, experimentation, data analysis, and writing original draft; S. I.-L.: conceptualization, experimentation, data analysis, investigation, and writing original draft; A. J.: conceptualization, experimentation, data analysis, investigation; M. T. L.-L.: experiment design, funding acquisition, and data analysis; J. M. C.: data analysis; V. B.: funding acquisition; J. A. G.: conceptualization, formal analysis, and writing – original draft; L. A. C.: conceptualization, funding acquisition, project administration, supervision, writing – original draft, and writing – review & editing; J. H.: conceptualization, funding acquisition, methodology, project administration, supervision, writing – original draft, and writing – review & editing.

Conflicts of interest

The authors declare no competing financial interest.

Data availability

The data supporting this article have been included as part of the supplementary information (SI). Supplementary information: Fig. S1: Characterization of the composite hydrogels (ASH) formed with a ratio of 3.5 : 1.5 : 5 of Fmoc-FF, Fmoc-RGD and collagen. Fig. S2: Additional characterisation of the composite hydrogels. Fig. S3: EDX analysis of the composite hydrogel. Fig. S4: Equilibrium water content (EWC) of ASNH-13 and ASNH-19 hydrogels Fig. S5: Antifungal activity of the hydrogels and live/dead assay against *C. albicans* AB226. Fig. S6: Confocal microscopy images of Amphotericin B treated polymicrobial biofilm. Fig. S7: *In vivo* biocompatibility of the hydrogels. See DOI: https://doi.org/10.1039/d5bm00761e.

References

1 R. Laxminarayan, A. Duse, C. Wattal, A. K. M. Zaidi, H. F. L. Wertheim, N. Sumpradit, E. Vlieghe, G. L. Hara, I. M. Gould, H. Goossens, C. Greko, A. D. So, M. Bigdeli, G. Tomson, W. Woodhouse, E. Ombaka, A. Q. Peralta, F. N. Qamar, F. Mir, S. Kariuki, Z. A. Bhutta, A. Coates, R. Bergstrom, G. D. Wright, E. D. Brown and O. Cars, Antibiotic resistance-the need for global solutions., *Lancet Infect. Dis.*, 2013, **13**, 1057–1098.

2 D. M. Morens, G. K. Folkers and A. S. Fauci, Emerging infections: a perpetual challenge., *Lancet Infect. Dis.*, 2008, **8**, 710–719.

3 M. M. Konai, B. Bhattacharjee, S. Ghosh and J. Haldar, Recent Progress in Polymer Research to Tackle Infections and Antimicrobial Resistance, *Biomacromolecules*, 2018, **19**, 1888–1917.

4 M. McKenna, Antibiotic resistance: the last resort, 2013, preprint, DOI: 10.1038/499394a.

5 C. Walsh, Molecular mechanisms that confer antibacterial drug resistance, *Nature*, 2000, **406**, 775–781.

6 S. K. Fridkin and W. R. Jarvis, Epidemiology of nosocomial fungal infections, *Clin. Microbiol. Rev.*, 1996, **9**, 499–511.

7 O. Ciofu, C. Moser, P. Ø. Jensen and N. Høiby, Tolerance and resistance of microbial biofilms, *Nat. Rev. Microbiol.*, 2022, **20**, 621–635.

8 H. C. Flemming, E. D. van Hullebusch, T. R. Neu, P. H. Nielsen, T. Seviour, P. Stoodley, J. Wingender and S. Wuertz, The biofilm matrix: multitasking in a shared space, *Nat. Rev. Microbiol.*, 2023, **21**, 70–86.

9 K. R. Eichelberger, S. Paul, B. M. Peters and J. E. Cassat, Candida – bacterial cross-kingdom interactions, *Trends Microbiol.*, 2023, **31**, 1287–1299.

10 V. T. Anju, S. Busi, M. Imchen, R. Kumavath, M. S. Mohan, S. A. Salim, P. Subhaswaraj and M. Dyavaiah, Polymicrobial Infections and Biofilms: Clinical Significance and Eradication Strategies, *Antibiotics*, 2022, **11**, 1731.

11 M. M. Harriott and M. C. Noverr, Importance of Candida-bacterial polymicrobial biofilms in disease, *Trends Microbiol.*, 2011, **19**, 557–563.

12 S. Chernousova and M. Epple, Silver as antibacterial agent: ion, nanoparticle, and metal, *Angew. Chem., Int. Ed.*, 2013, **52**, 1636–1653.

13 P. Dallas, V. K. Sharma and R. Zboril, Silver polymeric nanocomposites as advanced antimicrobial agents: classification, synthetic paths, applications, and perspectives, *Adv. Colloid Interface Sci.*, 2011, **166**, 119–135.

14 A. Agarwal, K. M. Guthrie, C. J. Czuprynski, M. J. Schurr, J. F. McAnulty, C. J. Murphy and N. L. Abbott, Polymeric Multilayers that contain Silver Nanoparticles can be Stamped onto Biological Tissues to Provide Antibacterial Activity, *Adv. Funct. Mater.*, 2011, **21**, 1863–1873.

15 F. G. Santos, L. C. Bonkovoski, F. P. Garcia, T. S. P. Cellet, M. A. Witt, C. V. Nakamura, A. F. Rubira and E. C. Muniz, Antibacterial Performance of a PCL-PDMAEMA Blend Nanofiber-Based Scaffold Enhanced with Immobilized Silver Nanoparticles, *ACS Appl. Mater. Interfaces*, 2017, **9**, 9304–9314.

16 A. Kumar, P. K. Vemula, P. M. Ajayan and G. John, Silver-nanoparticle-embedded antimicrobial paints based on vegetable oil, *Nat. Mater.*, 2008, **7**, 236–241.

17 J. A. Lemire, J. J. Harrison and R. J. Turner, Antimicrobial activity of metals: mechanisms, molecular targets and applications, *Nat. Rev. Microbiol.*, 2013, **11**, 371–384.

18 Z. M. Xiu, Q. B. Zhang, H. L. Puppala, V. L. Colvin and P. J. J. Alvarez, Negligible particle-specific antibacterial activity of silver nanoparticles, *Nano Lett.*, 2012, **12**, 4271–4275.

19 A. Zille, M. M. Fernandes, A. Francesko, T. Tzanov, M. Fernandes, F. R. Oliveira, L. Almeida, T. Amorim, N. Carneiro, M. F. Esteves and A. P. Souto, Size and Aging Effects on Antimicrobial Efficiency of Silver Nanoparticles Coated on Polyamide Fabrics Activated by Atmospheric DBD Plasma, *ACS Appl. Mater. Interfaces*, 2015, **7**, 13731–13744.

20 P. Yuan, X. Ding, Y. Y. Yang and Q.-H. Xu, Metal Nanoparticles for Diagnosis and Therapy of Bacterial Infection, *Adv. Healthcare Mater.*, 2018, **7**, e1701392.

21 I. Irwansyah, Y.-Q. Li, W. Shi, D. Qi, W. R. Leow, M. B. Y. Tang, S. Li and X. Chen, Gram-positive anti-microbial activity of amino acid-based hydrogels, *Adv. Mater.*, 2015, **27**, 648–654.

22 K. Yang, Q. Han, B. Chen, Y. Zheng, K. Zhang, Q. Li and J. Wang, Antimicrobial hydrogels: Promising materials for medical application, *Int. J. Nanomed.*, 2018, **13**, 2217–2263.

23 S. Li, S. Dong, W. Xu, S. Tu, L. Yan, C. Zhao, J. Ding and X. Chen, Antibacterial Hydrogels, *Adv. Sci.*, 2018, **5**, 1700527.

24 A. K. Nguyen, T. G. Molley, E. Kardia, S. Ganda, S. Chakraborty, S. L. Wong, J. Ruan, B. E. Yee, J. Mata, A. Vijayan, N. Kumar, R. D. Tilley, S. A. Waters and K. A. Kilian, Hierarchical assembly of tryptophan zipper peptides into stress-relaxing bioactive hydrogels, *Nat. Commun.*, 2023, **14**, 6604.

25 B. Adhikari and A. Banerjee, Short-peptide-based hydrogel: A template for the in situ synthesis of fluorescent silver nanoclusters by using sunlight, *Chem. – Eur. J.*, 2010, **16**, 13698–13705.

26 J. Song, C. Yuan, T. Jiao, R. Xing, M. Yang, D. J. Adams and X. Yan, Multifunctional Antimicrobial Biometallohydrogels Based on Amino Acid Coordinated Self-Assembly, *Small*, 2020, **16**, e1907309.

27 A. Levin, T. A. Hakala, L. Schnaider, G. J. L. Bernardes, E. Gazit and T. P. J. Knowles, Biomimetic peptide self-assembly for functional materials, *Nat. Rev. Chem.*, 2020, **4**, 615–634.

28 E. R. Draper and D. J. Adams, Low-Molecular-Weight Gels: The State of the Art, *Chem*, 2017, **3**, 390–410.

29 M. Aviv, M. Halperin-Sternfeld, I. Grigoriants, L. Buzhansky, I. Mironi-Harpaz, D. Seliktar, S. Einav, Z. Nevo and L. Adler-Abramovich, Improving the Mechanical Rigidity of Hyaluronic Acid by Integration of a Supramolecular Peptide Matrix, *ACS Appl. Mater. Interfaces*, 2018, **10**, 41883–41891.

30 M. Ghosh, M. Halperin-Sternfeld, I. Grinberg and L. Adler-Abramovich, Injectable alginate-peptide composite Hydrogel as a scaffold for bone tissue regeneration, *Nanomaterials*, 2019, **9**, 497.

31 Y. Yan, B. Cheng, K. Chen, W. Cui, J. Qi, X. Li and L. Deng, Enhanced Osteogenesis of Bone Marrow-Derived Mesenchymal Stem Cells by a Functionalized Silk Fibroin Hydrogel for Bone Defect Repair, *Adv. Healthcare Mater.*, 2019, **8**, 1801043.

32 B. Cheng, Y. Yan, J. Qi, L. Deng, Z. W. Shao, K. Q. Zhang, B. Li, Z. Sun and X. Li, Cooperative Assembly of a Peptide Gelator and Silk Fibroin Afford an Injectable Hydrogel for Tissue Engineering, *ACS Appl. Mater. Interfaces*, 2018, **10**, 12474–12484.

33 C. Gila-Vilchez, M. C. Mañas-Torres, Ó. D. García-García, A. Escribano-Huesca, L. Rodríguez-Arco, V. Carriel, I. Rodriguez, M. Alaminos, M. T. Lopez-Lopez and L. Álvarez de Cienfuegos, Biocompatible Short-Peptides Fibrin Co-assembled Hydrogels, *ACS Appl. Polym. Mater.*, 2023, **5**, 2154–2165.

34 R. M. Gouveia, R. R. Jones, I. W. Hamley and C. J. Connon, The bioactivity of composite Fmoc-RGDS-collagen gels, *Biomater. Sci.*, 2014, **2**, 1222–1229.

35 M. Zhou, A. M. Smith, A. K. Das, N. W. Hodson, R. F. Collins, R. V. Ulijn and J. E. Gough, Self-assembled peptide-based hydrogels as scaffolds for anchorage-dependent cells, *Biomaterials*, 2009, **30**, 2523–2530.

36 J. Nanda, B. Adhikari, S. Basak and A. Banerjee, Formation of hybrid hydrogels consisting of tripeptide and different silver nanoparticle-capped ligands: Modulation of the mechanical strength of gel phase materials, *J. Phys. Chem. B*, 2012, **116**, 12235–12244.

37 R. Contreras-Montoya, A. B. Bonhome-Espinosa, A. Orte, D. Miguel, J. M. Delgado-López, J. D. G. Duran, J. M. Cuerva, M. T. Lopez-Lopez and L. Álvarez de Cienfuegos, Iron nanoparticles-based supramolecular hydrogels to originate anisotropic hybrid materials with enhanced mechanical strength, *Mater. Chem. Front.*, 2018, **2**, 686–699.

38 M. C. Mañas-Torres, C. Gila-Vilchez, F. J. Vazquez-Perez, P. Kuzhir, D. Momier, J. C. Scimeca, A. Borderie, M. Goracci, F. Burel-Vandenbos, C. Blanco-Elices, I. A. Rodriguez, M. Alaminos, L. Álvarez de Cienfuegos and M. T. Lopez-Lopez, Injectable Magnetic-Responsive Short-Peptide Supramolecular Hydrogels: Ex Vivo and in Vivo Evaluation, *ACS Appl. Mater. Interfaces*, 2021, **13**, 49692–49704.

39 Md. W. Rahman, M. C. Mañas-Torres, S. Firouzeh, J. M. Cuerva, L. Álvarez de Cienfuegos and S. Pramanik, Molecular Functionalization and Emergence of Long-Range Spin-Dependent Phenomena in Two-Dimensional Carbon Nanotube Networks, *ACS Nano*, 2021, **15**, 20056–20066.

40 Md. W. Rahman, M. C. Mañas-Torres, S. Firouzeh, S. Illescas-Lopez, J. M. Cuerva, M. T. Lopez-Lopez, L. Á. de Cienfuegos, S. Pramanik, L. Alvarez de Cienfuegos and S. Pramanik, Chirality-Induced Spin Selectivity in Heterochiral Short-Peptide–Carbon-Nanotube Hybrid Networks: Role of Supramolecular Chirality, *ACS Nano*, 2022, **16**, 16941–16953.

41 B. Adhikari and A. Banerjee, Short peptide based hydrogels: Incorporation of graphene into the hydrogel, *Soft Matter*, 2011, **7**, 9259–9266.

42 Z. A. C. Schnepp, R. Gonzalez-McQuire and S. Mann, Hybrid biocomposites based on calcium phosphate mineralization of self-assembled supramolecular hydrogels, *Adv. Mater.*, 2006, **18**, 1869–1872.

43 M. Ghosh, M. Halperin-Sternfeld, I. Grigoriants, J. Lee, K. T. Nam and L. Adler-Abramovich, Arginine-presenting peptide hydrogels decorated with hydroxyapatite as biomimetic scaffolds for bone regeneration, *Biomacromolecules*, 2017, **18**, 3541–3550.

44 M. C. Mañas-Torres, G. B. Ramírez-Rodríguez, J. I. Garcia-Peiro, B. Parra-Torrejón, J. M. Cuerva, M. T. Lopez-Lopez, L. Alvarez de Cienfuegos and J. M. Delgado-López, Organic/Inorganic hydrogels by simultaneous self-assembly and mineralization of aromatic short-peptides, *Inorg. Chem. Front.*, 2022, **9**, 743–752.

45 M. Conejero-Muriel, R. Contreras-Montoya, J. J. Diaz-Mochon, L. Alvarez de Cienfuegos and J. A. Gavira, Protein crystallization in short-peptide supramolecular hydrogels: a versatile strategy towards biotechnological composite materials, *CrystEngComm*, 2015, **17**, 8072–8078.

46 R. Contreras-Montoya, M. Arredondo-Amador, G. Escolano-Casado, M. C. Mañas-Torres, M. González, M. Conejero-Muriel, V. Bhatia, J. J. Diáz-Mochón, O. Martínez-Augustin, F. S. De Medina, M. T. Lopez-Lopez, F. Conejero-Lara, J. A. Gavira and L. Álvarez de Cienfuegos, Insulin Crystals Grown in Short-Peptide Supramolecular Hydrogels Show Enhanced Thermal Stability and Slower Release Profile, *ACS Appl. Mater. Interfaces*, 2021, **13**, 11672–11682.

47 M. Conejero-Muriel, J. A. Gavira, E. Pineda-Molina, A. Belsom, M. Bradley, M. Moral, J. D. G. López-Durán, A. Luque González, J. J. Díaz-Mochón, R. Contreras-Montoya, Á. Martínez-Peragón, J. M. Cuerva and L. Álvarez De Cienfuegos, Influence of the chirality of short peptide supramolecular hydrogels in protein crystallogenesis, *Chem. Commun.*, 2015, **51**, 3862–3865.

48 Z. Batool, G. Muhammad, M. M. Iqbal, M. S. Aslam, M. A. Raza, N. Sajjad, M. Abdullah, N. Akhtar, A. Syed, A. M. Elgorban, S. S. Al-Rejaie and Z. Shafiq, Hydrogel assisted synthesis of gold nanoparticles with enhanced microbicidal and in vivo wound healing potential, *Sci. Rep.*, 2022, **12**, 1–10.

49 B. Nutan, A. K. S. Chandel, A. Biswas, A. Kumar, A. Yadav, P. Maiti and S. K. Jewrajka, Gold Nanoparticle Promoted Formation and Biological Properties of Injectable Hydrogels, *Biomacromolecules*, 2020, **21**, 3782–3794.

50 S. Palomba, L. Novotny and R. E. Palmer, Blue-shifted plasmon resonance of individual size-selected gold nanoparticles, *Opt. Commun.*, 2008, **281**, 480–483.

51 G. A. Vinnacombe-Willson, M. Núñez-Martínez, A. Herrero-Ruiz, F. Bevilacqua, R. Pazos, L. Troncoso-Afonso, M. Gallego-González, L. Scarabelli and L. M. Liz-Marzán, Plasmonic-Hydrogel Hybrid Biomaterials Via In Situ Seeded Growth, *Angew. Chem. Int. Ed.*, 2025, **64**, e202501854.

52 S. Adorinni, S. Gentile, O. Bellotto, S. Kralj, E. Parisi, M. C. Cringoli, C. Deganutti, G. Malloci, F. Piccirilli, P. Pengo, L. Vaccari, S. Geremia, A. V. Vargiu, R. De Zorzi and S. Marchesan, Peptide Stereochemistry Effects from pKa-Shift to Gold Nanoparticle Templating in a Supramolecular Hydrogel, *ACS Nano*, 2024, **18**, 3011–3022.

53 C. Stani, L. Vaccari, E. Mitri and G. Birarda, FTIR investigation of the secondary structure of type I collagen: New insight into the amide III band, *Spectrochim. Acta, Part A*, 2020, **229**, 1–7.

54 A. B. Bonhome-Espinosa, F. Campos, I. A. Rodriguez, V. Carriel, J. A. Marins, A. Zubarev, J. D. G. Duran and M. T. Lopez-Lopez, Effect of particle concentration on the microstructural and macromechanical properties of biocompatible magnetic hydrogels, *Soft Matter*, 2017, **13**, 2928–2941.

55 D. Borin, D. Günther, C. Hintze, G. Heinrich and S. Odenbach, The level of cross-linking and the structure of anisotropic magnetorheological elastomers, *J. Magn. Magn. Mater.*, 2012, **324**, 3452–3454.

56 Y. P. Moreno Ruiz, L. A. de Almeida Campos, M. A. Alves Agreles, A. Galembeck and I. Macário Ferro Cavalcanti, Advanced Hydrogels Combined with Silver and Gold Nanoparticles against Antimicrobial Resistance, *Antibiotics*, 2023, **12**, 104.

57 H. D. A. Weerasekera, M. J. Silvero, D. Regis Correa Da Silva and J. C. Scaiano, A database on the stability of silver and gold nanostructures for applications in biology and bio-molecular sciences, *Biomater. Sci.*, 2017, **5**, 89–97.

58 M. J. Reiniers, R. F. Van Golen, S. Bonnet, M. Broekgaarden, T. M. Van Gulik, M. R. Egmond and M. Heger, Preparation and Practical Applications of 2′,7′-Dichlorodihydrofluorescein in Redox Assays, *Anal. Chem.*, 2017, **89**, 3853–3857.

59 T. G. Dong, S. Dong, C. Catalano, R. Moore, X. Liang and J. J. Mekalanos, Generation of reactive oxygen species by lethal attacks from competing microbes, *Proc. Natl. Acad. Sci. U. S. A.*, 2015, **112**, 2181–2186.

60 H. Li, X. Zhou, Y. Huang, B. Liao, L. Cheng and B. Ren, Reactive Oxygen Species in Pathogen Clearance: The Killing Mechanisms, the Adaption Response, and the Side Effects, *Front. Microbiol.*, 2021, **11**, 622534.

61 J. A. Buttress, M. Halte, J. D. te Winkel, M. Erhardt, P. F. Popp and H. Strahl, A guide for membrane potential measurements in Gram-negative bacteria using voltage-sensitive dyes, *Microbiology*, 2022, **168**, 001227.

62 S. Mukherjee, S. Barman, R. Mukherjee and J. Haldar, Amphiphilic Cationic Macromolecules Highly Effective Against Multi-Drug Resistant Gram-positive Bacteria and Fungi With No Detectable Resistance, *Front. Bioeng. Biotechnol.*, 2020, **8**, 1–19.

63 M. C. Fisher, A. Alastruey-Izquierdo, J. Berman, T. Bicanic, E. M. Bignell, P. Bowyer, M. Bromley, R. Brüggemann, G. Garber, O. A. Cornely, S. J. Gurr, T. S. Harrison, E. Kuijper, J. Rhodes, D. C. Sheppard, A. Warris, P. L. White, J. Xu, B. Zwaan and P. E. Verweij, Tackling the emerging threat of antifungal resistance to human health, *Nat. Rev. Microbiol.*, 2022, **20**, 557–571.

64 A. Ganesan, F. Shaikh, W. Bradley, D. M. Blyth, D. Bennett, J. L. Petfield, M. L. Carson, J. M. Wells and D. R. Tribble, Classification of trauma-associated invasive fungal infections to support wound treatment decisions, *Emerging Infect. Dis.*, 2019, **25**, 1639–1647.

65 S. Ghosh, M. Zheng, J. He, Y. Wu, Y. Zhang, W. Wang, J. Shen, K. W. K. Yeung, P. Neelakantan, C. Xu and W. Qiao, Electrically-driven drug delivery into deep cutaneous tissue by conductive microneedles for fungal infection eradication and protective immunity, *Biomaterials*, 2025, **314**, 122908.

66 P. G. Pappas, M. S. Lionakis, M. C. Arendrup, L. Ostrosky-Zeichner and B. J. Kullberg, Invasive candidiasis, *Nat. Rev. Dis. Primers*, 2018, **4**, 18026.

67 S. Barman, S. Mukherjee, B. Bhattacharjee, K. De, R. Mukherjee and J. Haldar, Biocide loaded shear-thinning hydrogel with anti-biofilm efficacy cures topical infection, *Biomater. Sci.*, 2023, **11**, 998–1012.

68 S. Mukherjee, S. V. Shinde, P. Talukdar and J. Haldar, Unveiling the potent activity of a synthetic ion transporter against multidrug-resistant Gram-positive bacteria and biofilms, *RSC Med. Chem.*, 2024, **15**, 2127–2137.

69 S. Mukherjee, S. Ghosh and J. Haldar, Amphiphilic cationic macromolecule potentiates tetracycline against multi-drug resistant Gram-negative bacteria, *Bull. Mater. Sci.*, 2020, **43**, 311.

70 S. Ghosh, R. Mukherjee, S. Mukherjee, S. Barman and J. Haldar, Engineering Antimicrobial Polymer Nanocomposites: In Situ Synthesis, Disruption of Polymicrobial Biofilms, and in Vivo Activity, *ACS Appl. Mater. Interfaces*, 2022, **14**, 34527–34537.

71 R. Dey, S. Mukherjee, R. Mukherjee and J. Haldar, Small molecular adjuvants repurpose antibiotics towards Gram-negative bacterial infections and multispecies bacterial biofilms, *Chem. Sci.*, 2024, **15**, 259–270.

72 S. Barman, R. Dey, S. Ghosh, R. Mukherjee, S. Mukherjee and J. Haldar, Amino Acid-Conjugated Polymer-Silver Bromide Nanocomposites for Eradicating Polymicrobial Biofilms and Treating Burn Wound Infections, *ACS Infect. Dis.*, 2024, **10**, 2999–3012.

73 S. Mukherjee, S. Chakravarty and J. Haldar, Revitalizing Antibiotics with Macromolecular Engineering: Tackling Gram-Negative Superbugs and Mixed Species Bacterial Biofilm Infections In Vivo, *Biomacromolecules*, 2025, **26**, 2211–2226.

74 R. Dey, R. Mukherjee, S. Mukherjee and J. Haldar, Bactericidal Hemostatic Sponge: A Point of Care Solution to Combat Traumatic Injury, *Adv. Healthcare Mater.*, 2025, **2404176**, 1–13.